GA–A23232

EFFECTS OF IMPURITY SEEDING IN DIII–D RADIATING MANTLE DISCHARGES

by
G.L. JACKSON, M. MURAKAMI, G.R. McKEE, D.R. BAKER, J.A. BOEDO,
R.J. LA HAYE, C.J. LASNIER, A.W. LEONARD, A.M. MESSIAEN,
J. ONGENA, G.M. STAEBLER, B. UNTERBERG, M.R. WADE,
J.G. WATKINS, and W.P. WEST

This is a preprint of a paper submitted for publication in *Nucl. Fusion.*

MAY 2000

DISCLAIMER

GA–A23232

EFFECTS OF IMPURITY SEEDING IN DIII–D RADIATING MANTLE DISCHARGES

by
G.L. JACKSON, M. MURAKAMI,* G.R. McKEE,† D.R. BAKER, J.A. BOEDO,‡
R.J. LA HAYE, C.J. LASNIER,# A.W. LEONARD, A.M. MESSIAEN,△
J. ONGENA,△ G.M. STAEBLER, B. UNTERBERG,¶ M.R. WADE,*
J.G. WATKINS,§ and W.P. WEST

This is a preprint of a paper submitted for publication in *Nucl. Fusion.*

*Oak Ridge National Laboratory, Oak Ridge, Tennessee.
†University of Wisconsin, Madison, Wisconsin.
‡University of California, San Diego, California.
#Lawrence Livermore National Laboratory, Livermore, California.
△Association EURATOM, Ecoloe Royal Militaire, Brussels, Belgium.
¶Assodation EURATOM, Jülich, Germany.
§Sandia National Laboratory, Albuquerque, New Mexico.

Work supported by
the U.S. Department of Energy under
Contract No. DE-AC03-99ER54463

GA PROJECT 30033
MAY 2000

ABSTRACT

Impurity injection, with neon, argon, or krypton, has been used in DIII-D to increase radiation in the mantle region, with confinement enhancements above the ITERL-89P L–mode scaling relation in both diverted and limited discharges. For discharges with an L–mode edge (both limited and diverted), impurity injection produces a prompt increase in confinement (solid line) and a more gradual increase in density. These changes occur at densities and radiated power fractions significantly lower than observed in the TEXTOR tokamak device. ELMing H–mode discharges with active pumping and high deuterium gas feed (puff and pump) exhibit an increase in density with no decrease in energy confinement after impurity injection, increasing to near the Greenwald density limit following a spontaneous transition several hundred milliseconds after impurity injection. The highest density phase of these discharges is usually terminated after the onset of n=2 MHD activity, identified as an m/n = 3/2 neoclassical tearing mode. High performance discharges at lower density have also been achieved, with a reduction the edge electron pressure and the edge electron pressure gradient and longer ELM-free periods than in comparable discharges without impurity seeding. A reduction in density fluctuations after impurity injection in the mantle region has been measured by beam emission spectroscopy (BES) in L–mode discharges. A reduction in ion temperature driven (ITG) modes is calculated for these discharges, consistent with the observed BES measurements and is the leading candidate to explain the observed confinement improvements.

TABLE OF CONTENTS

TABLE OF CONTENTS (CONTINUED)

LIST OF FIGURES

LIST OF FIGURES (CONTINUED)

I. INTRODUCTION

Intrinsic impurities in tokamak discharges, namely carbon, oxygen, and medium or high Z metals, have generally been regarded as deleterious to sustained high performance and reproducible discharges. However *non-intrinsic* impurities have been shown, under some conditions, to produce confinement improvements above low mode (L–mode) [1] scaling and the radiating mantle which can accompany these impurities can minimize peak heat flux to plasma facing components: an important design consideration for fusion ignition devices. We report in this paper on a series of experiments in DIII–D to explore the role of non-intrinsic impurity gases, i.e. neon, argon, and krypton, in DIII–D discharges with confinement enhancements above L–mode.

Several tokamaks have previously reported improved confinement with injection of neon or other impurities [2–8]. The first such studies were for the Z–mode on ISX-B [2] and the effect has been most extensively documented in the TEXTOR tokamak [3, 9–11]. The TEXTOR group has developed a simple scaling for their radiative improved mode (RI–mode) discharges [3], namely

$$\tau_{RI-mode}/\tau_{ITERH-93P} = c_1 \times \bar{n}_e / n_{GW} \quad , \tag{1}$$

where constant c_1 is approximately unity, $\tau_{ITERH-93P}$ is the ELM-free H–mode confinement scaling relation [12], and the Greenwald density limit [13] is defined as n_{GW} (10^{20} m^{-3}) = I_p (MA)/(π a^2). Both ISX-B and TEXTOR have nearly circular cross section, a poloidal limiter, and operate with an L–mode edge. Non-intrinsic impurities have also been injected into diverted devices with an H–mode edge in ASDEX–U, JFT–2M, JET, and DIII–D (prior to the experiments described here). Confinement enhancements above L–mode were obtained in all of these devices, but often there was a confinement degradation when compared to H–mode scaling relations, particularly at the highest densities. Although the effect of improved confinement with impurity seeding has been observed and well documented on many devices, the underlying physical mechanisms responsible for this improvement have not been well understood.

The goals of the experiments reported here are: (1) obtain enhanced confinement discharges in DIII–D with a large fraction of radiated power in the mantle region, (2) extend the results of TEXTOR to a larger machine, providing size scaling, (3) explore the parameter range in which these impurity seeded discharges with enhanced confinement

can be obtained, and (4) evaluate the physical mechanisms leading to improved confinement with impurity seeding.

In this paper we will describe impurity seeded discharges with enhanced confinement, defined as confinement above L–mode scaling. As discussed below the degree of confinement enhancement is a function of many variables and we will quantify this for the various types of discharges presented in this paper. To represent the data in this paper, we compare measured confinement values to either the ITERL–89P L–mode [1] or ITERH–93P ELM-free H–mode [12] scaling relations. We will sometimes apply the ITERH–93P ELM-free scaling relation to L–mode discharges with impurity seeding because this will allow comparison to other devices which have used this scaling in the literature. To provide a comparison between these scaling relations applied to typical DIII–D discharges with impurity seeding, the scaling relations (L–mode[1] and ELM-free H–mode [12]) are given in Table I.

TABLE I
NORMALIZED CONFINEMENT FACTORS FOR TYPICAL DIII-D DISCHARGES WITH IMPURITY SEEDING

	$\tau_E/\tau_{ITERL-89P}$	$\tau_E/\tau_{ITERH-93P}$
Puff and pump H–mode (argon) #95891	1.63	1.04
Inner wall limited L–mode (neon) #98795	1.79	1.45
VH–mode (neon) #96568	2.60	1.93

DIII–D discharges with non-intrinsic radiation have been obtained under a variety of conditions and in various configurations. In this paper we will focus on three types of discharges: lower single-null (LSN) puff and pump ELMing H–mode, L–mode (either inner wall limited (IWL) or upper single-null (USN) divertor), and double-null divertor (DND) high performance, $H_{89P} > 2$, where the L–mode confinement enhancement factor, $H_{89P} = \tau_E/\tau_{ITERL-89P}$. We will similarly define the H–mode confinement enhancement factor as $H_{93P} = \tau_E/\tau_{ITERH-93P}$. In all discharges discussed in this paper, the $\nabla \mathbf{B} \times \mathbf{B}$ drift direction is toward the floor, e.g. the drift is away from the X–point in an USN divertor configuration. he temporal evolution in normalized density and normalized confinement space for a typical discharge of each type is shown in Fig. 1.

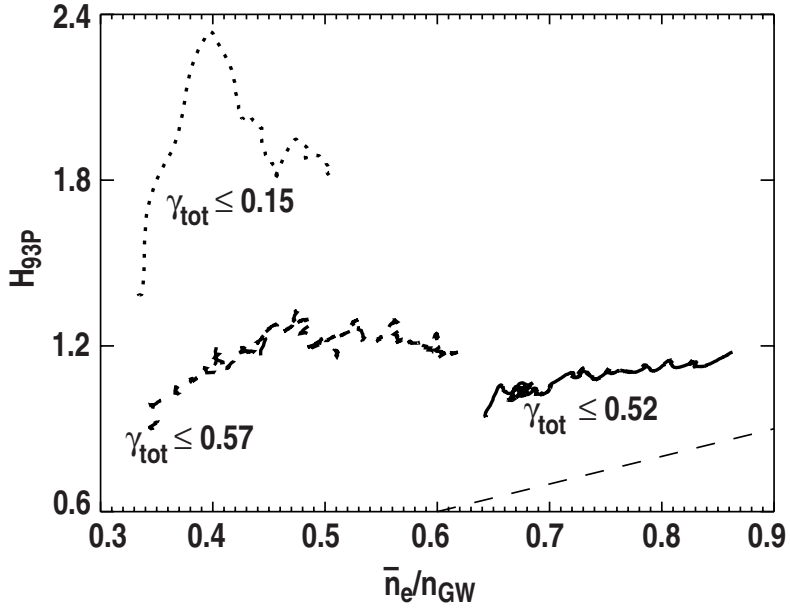

Fig. 1. Phase space diagram for the temporal evolution of three impurity seeded discharges typical of the three types discussed in this paper: puff and pump ELMing H–mode (#95020), solid; L–mode edge (#98347), dash; and high performance, (#96568), dot. TEXTOR RI–mode scaling, Eq. (1) is shown as a dashed line. The radiative power fraction, γ_{tot}, is defined in Section I.

In this paper we will focus on discharges in which impurity injection leads to increased radiation in the mantle region and improved confinement in the core. The pathological case where the core temperature cools and impurity radiation peaks on axis is not discussed here. Impurity seeded discharges where impurity radiation is primarily in the *divertor* region have been reported previously [14] and except for comparisons, they are not presented in this paper. Throughout this paper we define the mantle region of a discharge as $0.5 \leqq \rho \leqq 1.0$ and the core region as $\rho < 0.5$, where ρ is the normalized radius. We define the fraction of core, mantle, divertor, and total radiated power as $\gamma_{core} = P_{core}/P_{in}$, $\gamma_{mantle} = P_{mantle}/P_{in}$, $\gamma_{div} = P_{div}/P_{in}$, $\gamma_{tot} = P_{tot}/P_{in}$, respectively. No rf heating was used for the discharges described in this paper so the input power is $P_{in} = P_{NB}$ P_{ohmic} where P_{NB} and P_{ohmic} are the neutral beam and ohmic heating power respectively.

In Sections II through IV we will discuss the characteristics of the three types of impurity seeded discharges shown in Fig. 1, focusing on specific discharges which are typical for each type. Various aspects of these discharge types are discussed, i.e. radiation, global confinement, transport, scaling, and impurities, although due to diagnostic limitations, not all topics are covered in all sections. A discussion of the experimental results, comparison to other machines, and conclusions is contained in Section V.

II. IMPURITY SEEDING IN PUFF AND PUMP ELMING H–MODE DISCHARGES

Impurity seeding has been applied to ELMing H–mode discharges with a high deuterium flow, resulting in no loss of H–mode confinement and in some cases a small increase. After impurity injection, density increases and a spontaneous transition, described later, is sometimes observed. In the following discussion we will describe changes in the mantle, the core, and the H–mode transport barrier regions with impurity seeding.

Both radiating mantle and radiating divertor discharges have been observed under conditions of high deuterium gas flow and impurity injection. These impurity entrainment experiments used non-intrinsic impurities as a means to obtain a high radiative fraction without a large increase in core impurities and were accomplished by utilizing a large deuterium gas flow such that the frictional force associated with this flow is larger than the thermal gradient force. The divertor strike point is positioned near the entrance to the toroidally continuous liquid helium cryopump for particle removal. This technique is referred to as puff and pump [14], and the geometry is shown in Fig. 2. While the original goal of these experiments was to produce a highly radiating divertor, e.g. Fig. 2(b), some discharges instead exhibited a radiating mantle, e.g. Fig. 2(a).

A Temporal evolution of ELMing H–mode discharges with argon injection

Two discharges with impurity seeding are compared to a puff and pump reference discharge in Fig. 3. All had a high deuterium gas flow [Fig. 3(e)] and during the interval shown in Fig. 3 were in ELMing H–mode. Impurity seeded discharges at two power levels are displayed: the lower power level (dotted curves) shows a monotonic increase in $\bar{n}_e/n_{GW}$ and γ_{mantle} until a radiative collapse occurs at 3.8 s, while the discharge at higher power and argon injection rate exhibits higher normalized confinement (solid line) and a monotonic density increase, reaching $\bar{n}_e/n_{GW} \approx 0.9$ before the onset of n = 2 MHD activity. Although density can approach the Greenwald density limit in these puff and pump discharges, stored magnetic energy, W_{MHD}, and energy confinement time are the same, as, or higher than, discharges with no impurity seeding, e.g. Fig. 3(b). Note that even after the n = 2 MHD activity begins, density is still approximately 30% above the reference case and ELM-free H–mode confinement, $H_{93P} \geqq 1$, is maintained. In discharge #95011 there is a transition at 2.8–2.9 s where both density and γ_{mantle} begin

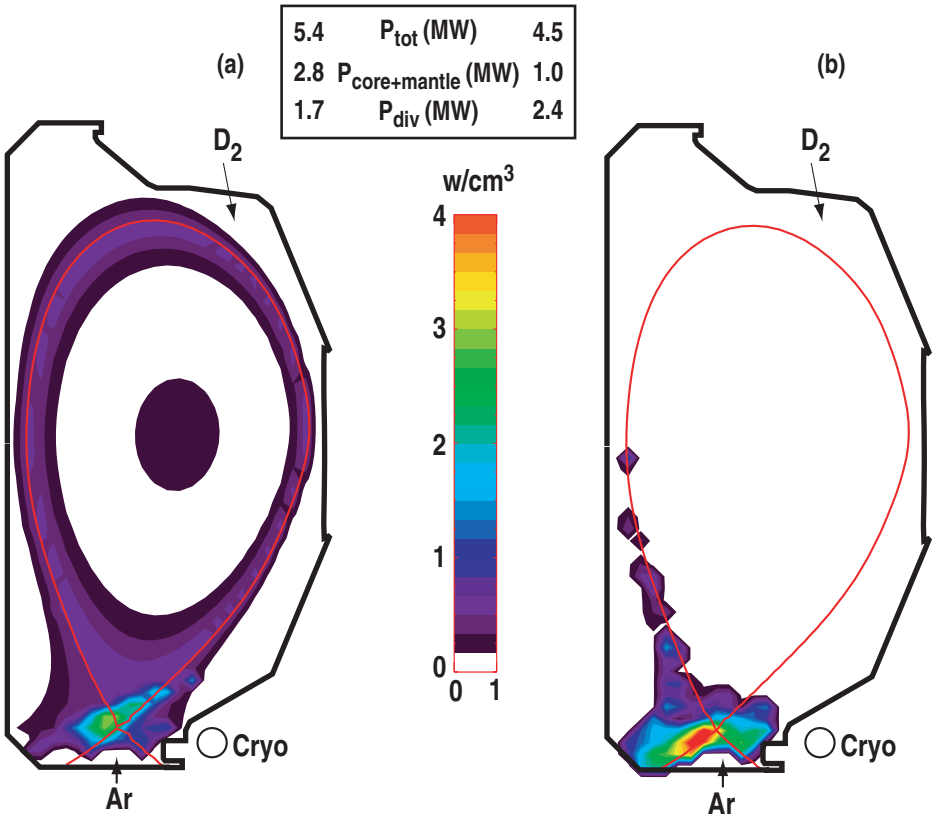

Fig. 2. Radiated power profiles at t = 3.24 s for two puff and pump discharges: (a) radiating mantle, #95011 , and (b) radiating divertor, #95012. Discharge parameters are I_p = 1.3 MA, B_T = 2.1 T, $\bar{P}_{nb}$ = 6.3 MW (a) and 6.7 MW (b). Argon and deuterium gas puffing rates were identical for these discharges.

increasing at a faster rate. A similar change in observed in discharge #96981 from 2.95 s to 3.1 s. We will refer to this as the spontaneous transition in this paper. and it will be discussed in more detail later. It is also characterized by an increase in toroidal rotation.

The two discharges in Fig. 3 at similar neutral beam heating power, one with and one without impurity seeding, are displayed in Fig. 4. The edge electron pedestal pressure and density, P_e^{ped} [Fig. 4(a)] and n_e^{ped} [Fig. 4(b)], are calculated using a hyperbolic tangent fit function [15] to the Thomson scattering profile data. Using the formulation given by Fishpool [16], the pedestal stored energy, W_{ped}, shown in Fig. 4(c), is defined by the relation

$$W_{ped} = 2 \times P_e^{ped} \times V_p \qquad (2)$$

where V_p is the plasma volume in m^3 and using the assumption that $T_i = T_e$.

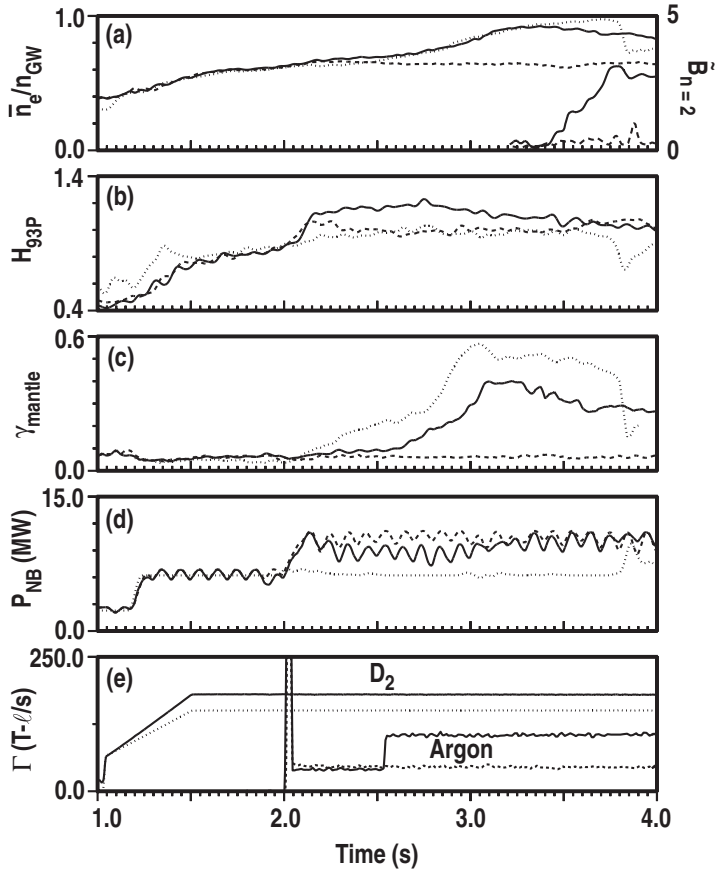

Fig. 3. Comparison of two argon impurity seeded discharges (solid, #96981, and dotted #95011) to a baseline discharge with no impurity injection (dashed, #96982). MHD activity (a) limits the maximum achievable density in #96981 (#95011 had no fast magnetic data at times near the maximum density). Normalized energy confinement is plotted in (b), the fraction of mantle radiation is shown in (c) and neutral beam auxiliary heating power in (d). Discharges #96981 and #96982 had the same rate of deuterium puffing, (e). Discharge parameters are: LSN divertor, I_p = 1.3 MA, B_T = 2.1 T.

After impurity injection there is only a small decrease in edge pedestal pressure and W_{ped} compared to the reference discharge ($W_{ped}/W_{MHD} \approx 0.2$). Note that although electron pedestal density is initially unchanged after impurity injection there is a sharp increase from 2.95 to 3.1 s associated with the spontaneous transition.

Both the ELM frequency and power flow across the last closed flux surface, P_{LCFS}, decrease after argon injection, plotted in Fig. 4(d) and 4(e), where

$$P_{LCFS} = P_{NB} + P_{ohmic} - dW_{MHD}/dt - P_{mantle} - P_{core} \quad . \tag{3}$$

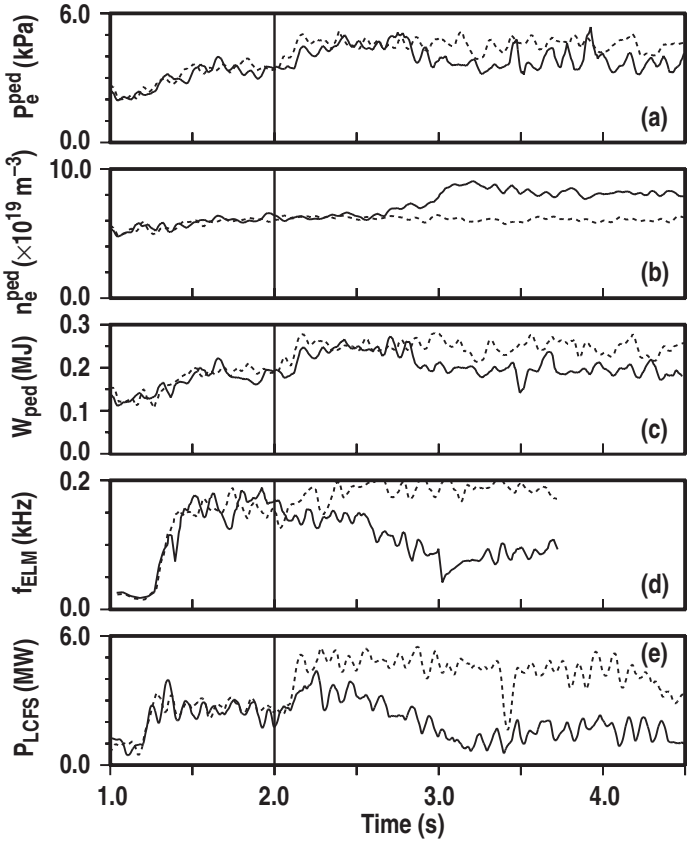

Fig. 4. Edge parameters for a radiating mantle discharge (solid line, 96981) and a baseline discharge (dashed, 96982). Shown are: (a) edge electron pedestal pressure, (b) pedestal density, (c) pedestal stored energy defined by Eq. (2), (d) ELM frequency, and (e) power flow across the LCFS. Discharge parameters are given in Fig. 3. Argon injection, indicated by a vertical line, begins at t = 2.0 s. The approximate time of the spontaneous transition is shown by cross hatches.

Although P_{LCFS} in puff and pump discharges decreases after impurity injection, significantly reducing power flow to the divertor, these discharges are not completely detached. Shown in Fig. 5 is the particle flux measured by the floor Langmuir probes near the position of peak heat flux [Fig. 5(c)] and in the outer scrape off [Fig. 5(d)]. The particle fluxes are averaged over 0.02 s, so transient ELM increases are not apparent. Both probes indicate a reduction in the particle flux after impurity injection. Reduced particle flux to the divertor tiles is consistent with a reduction in the peak power flow to these tiles, shown in Fig. 5(e). There is also a decrease in the total D_α line radiation both in the average value and the peak ELM amplitude, shown in Fig. 5(a). The total carbon III line emission, with the same filterscope viewing geometry, does not exhibit the same reduction after argon injection, although some reduction in peak amplitude is observed after the spontaneous transition [Fig. 5(b)]. The decrease in the observed D_α line intensity may be due to increasing particle confinement which reduces the incident flux of deuterons to the wall and hence the recycled deuterons. The physical mechanisms producing carbon in

DIII–D are not well understood, and no conclusions can be inferred about the wall carbon sources at this time.

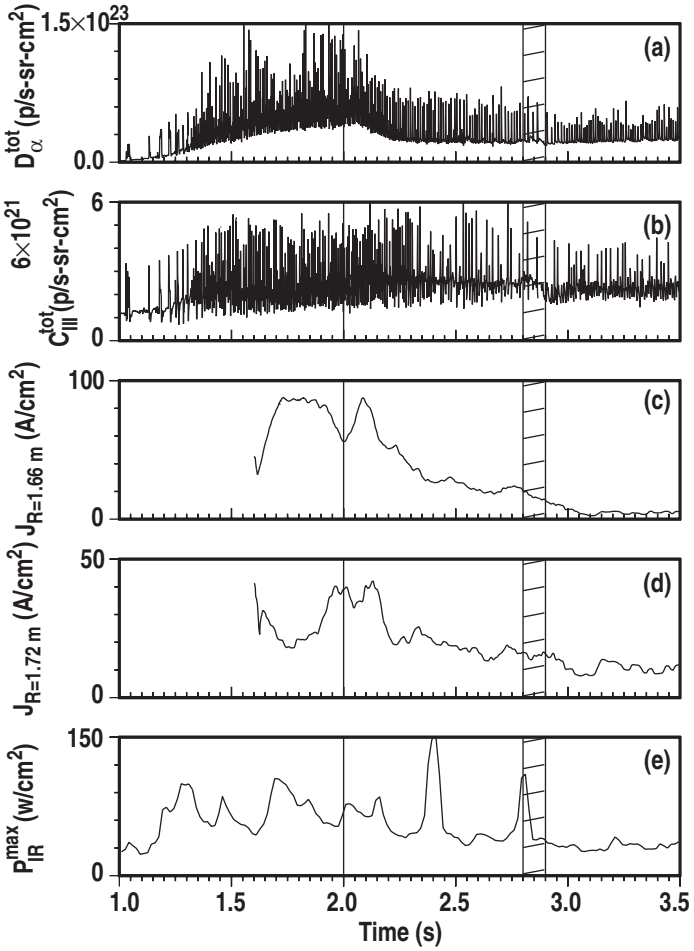

Fig. 5. SOL and recycling parameters for a radiating mantle discharge (#95011). (a) total deuterium recycling and (b) total CIII line emission are plotted before and during argon injection. Incident particle fluxes at the divertor floor are shown: (c) within 1 cm of the outer strike point, and (d) in the SOL near the entrance to the cryopump. Peak heat flux on the divertor tiles measured by an IRTV camera is plotted in (e).

B. Global scaling characteristics of puff and pump discharges with argon injection

Non-intrinsic impurities can also affect edge pressure gradients. Figure 6(a) shows the electron pedestal pressure, determined from a hyperbolic tangent fit to the edge electron profiles obtained from Thomson scattering [15]. This series of puff and pump discharges, including discharge #95011, had similar parameters (I_p, B_T and P_{NB}) and was obtained during one experimental day. Data near an ELM transition was excluded. There is a systematic decrease in the edge pedestal pressure as the radiated power fraction increases.

There is only a small decrease in H_{89P} at the highest radiated power, plotted in Fig. 6(b). The decrease in edge pressure suggests that impurity injection may be a useful tool for pressure profile control in future scenarios such as the DIII–D advanced tokamak program [17]. Modeling of similar discharges shows a reduction of edge bootstrap current with impurity puffing and the total edge toroidal current also decreased with increasing impurity injection.

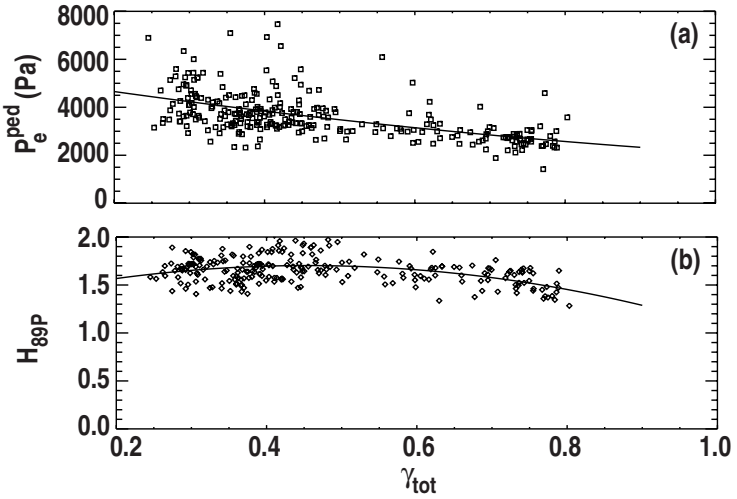

Fig. 6. Edge electron pedestal pressure (a) and normalized confinement (b) for puff and pump discharges during the time of argon injection is shown as a function of normalized radiated power. Data is from shot series #95007–95026 (I_p = 1.3 MA, B_T = 2.1 T, P_{NB} = 6–8 MW).

DIII–D puff and pump ELMing H–mode discharges allow operation at higher densities than unseeded discharges, shown in Fig. 7. The non-impurity discharges are taken from the DIII–D ITER ELMing H–mode database. In general, the argon discharges allow operation with confinement enhancements equivalent to ELMing H–mode at higher densities than normally obtained in DIII–D. We note that to date the *highest* density discharges with argon injection achieved in DIII–D are not steady state. However, quasi-stationary impurity seeded discharges have been obtained. One example is shown in Fig. 7 as solid circles, taken at two times (2.8 and 3.4 s). Many discharges, while not stationary, maintain good confinement as the density slowly increases over several confinement times. An example of this behavior is the puff and pump discharge shown in Fig. 1, where $0.75 \leqq \bar{n}_e/n_{GW} \leqq 0.87$ and $H_{93P} \geqq 1.1$ for a time, $\Delta t/\tau_E = 5.5$. The data with impurity seeding plotted in Fig. 7 shows no trend of increasing confinement with density and at a given density there are variations in H_{93P} from shot to shot of more than ±10%. The points displayed in this figure represent one or two times during the impurity seeded phase. However, as shown in Fig. 1, some puff and pump discharges do show modest

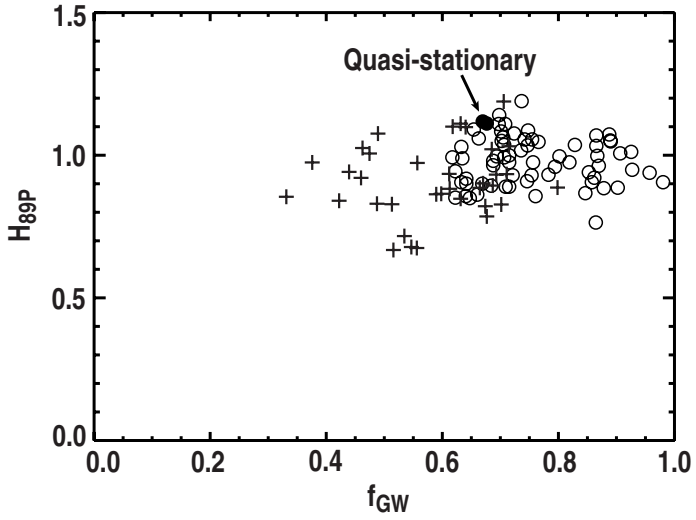

Fig. 7. Puff and Pump argon seeded discharges (circles) have been achieved at higher density than for comparable non-seeded DIII–D ELMing H–mode discharges (+ symbols) taken from the ITER ELMing database, $1.2 \leqq I_p \leqq 1.4$ MA. Two times during a steady state puff and pump argon seeded discharge are also displayed (solid circles).

increases in confinement as density increases during the impurity injection phase, although this behavior is not always observed and can be modified by the onset of saw-teeth or MHD modes.

C. Transport

Puff and pump discharges show a marked decrease in the effective thermal diffusivity with impurity injection with the largest change occurring in the mantle region. Reductions in other transport channels, e.g. momentum, are also observed, accompanied by an increase in the thermal neutron rate. The transport coefficients were calculated using the TRANSP code [18]. Inputs to this code are: T_e (Thomson scattering and third harmonic electron cyclotron Fourier spectrometer, HECE), n_e (Thomson scattering and four channel interferometer), T_i (charge exchange recombination, CER), radiated power (48 channel bolometer array), impurity density (SPRED UV spectrometer and CER), magnetic equilibria (magnetic probes and flux loops), current profile (35 channel motional Stark effect, MSE, array), and neutron emission, S_n.

The single fluid effective thermal diffusivity, χ_{eff}, is shown in Fig. 8(a) at $\rho = 0.7$ for a typical high density puff and pump discharge. This diffusivity decreases monotonically until the spontaneous transition, remaining constant at approximately twice the neoclassical value after that time. The largest change in the χ_{eff} profile occurs in the mantle region at approximately this normalized radius. The short electron-ion equilibration time in these

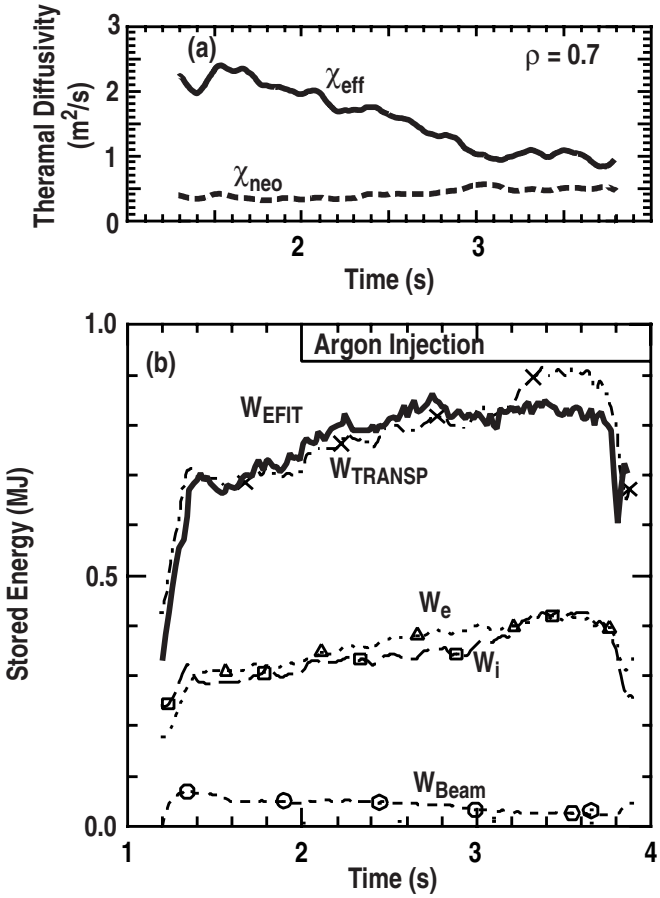

Fig. 8. χ_{eff} decreases after argon injection beginning at 2.0 s, (#95011, ρ = 0.7), (a). Total stored energy, W_{EFIT}, calculated from EFIT magnetic equilibria code (solid line) is compared to W_{TRANSP}, (b). The components W_e,W_i, and W_{beam} are also plotted.

high density discharges allows near equilibration between ions and electrons and $T_i \approx T_e$. Since the calculation of χ_{eff} has lower uncertainties than χ_i and χ_e, and χ_{eff} can be uniquely determined, it is presented in Fig. 8(a). However, it is clear that both χ_i and χ_e decrease after argon injection until the time of the spontaneous transition, 2.8 s. After this time, the ion thermal diffusivity rapidly decreases, while electron thermal diffusivity increases over the entire profile.

The total stored energy exhibits a modest increase after impurity injection begins at 2.0 s., shown in Fig. 8(b). W_{EFIT}, calculated by the EFIT magnetic equilibria code is compared to the stored energy, W_{TRANSP}, calculated from the TRANSP profile analysis and is good agreement. Also shown in Fig. 8(b) are the stored energy components contributing to the total stored energy from electrons, thermal ions, and fast ions. We note that the thermal component, $W_i + W_e$ is $\geqq$ 91% of the total during this discharge, i.e., the fast ion contribution is small. Thermal pressure profiles (not shown) indicate that the core

region exhibits the largest increase in both ion and electron pressure leading to the increase in stored energy described previously. After the spontaneous transition beginning at t ≈ 2.8 s, central ion pressure further increases while central electron pressure remains relatively constant.

Toroidal rotation increases after impurity injection and is most apparent after the spontaneous transition (Fig. 9). Since ion and electron density are also increasing, there is a net increase in plasma toroidal momentum. In addition to the steady increase in core toroidal rotation after impurity injection, there is also a large increase in core rotation, most apparent at $\rho = 0.03$ in Fig. 9 and beginning at 1.45 s, peaking at 1.78 s, and rapidly collapsing. This phenomena occurs before impurity injection and is observed even in some discharges without impurity puffing. The cause of this transient behavior has not yet been identified but it could be associated with the formation of an internal transport barrier (ITB) in the plasma core. This phenomena terminates before impurity injection and it will not be discussed further.

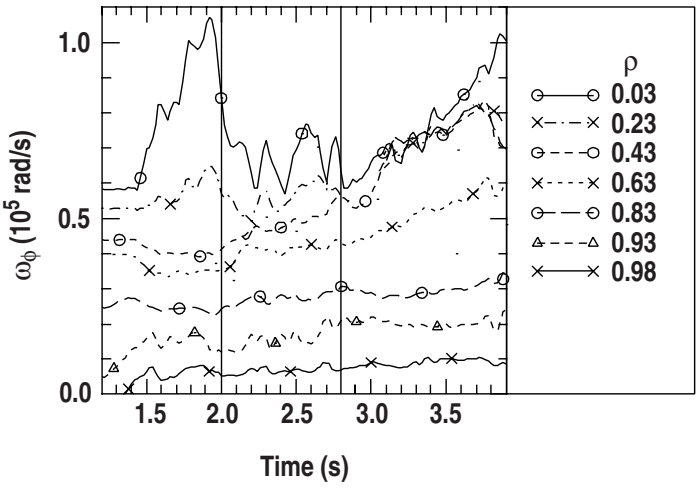

Fig. 9. Toroidal plasma rotation increases in the core region after argon injection at 2.0 s (#95011). Vertical lines show the beginning of impurity injection, 2.0 s, and the spontaneous transition.

Accompanying the increase in toroidal rotation is an increase in the **E**×**B** shearing rate, most pronounced in the mantle region [Fig. 10]. The shearing rate initially increases after argon injection begins at 2.0 s and another increase occurs after the spontaneous transition at 2.8–29 s. The higher **E**×**B** shearing rate can reduce the growth rate of microturbulence [19], may explain the observed decreases in χ_{eff}.

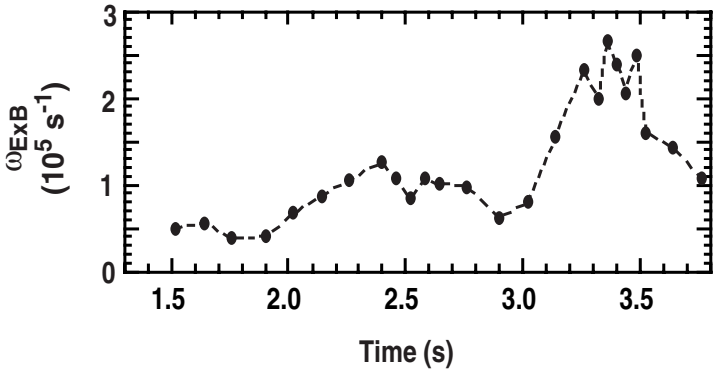

Fig. 10. **E×B** shearing rate as a function of time for discharge #95011 at $\rho = 0.7$.

D. Impurities in puff and pump ELMing H–mode discharges

The intentional introduction of impurities has the potential for increasing both Z_{eff} and dilution of the main species to unacceptable levels, lowering reactivity and neutron yield. Thus, core impurity concentration is an important consideration in these types of discharges.

Shown in Fig. 11 is Z_{eff}, calculated by the TRANSP code with measured impurity density profiles, for puff and pump discharge #95011. Although Z_{eff} increases after argon injection at 2.0 s, the profile is hollow and Z_{eff} actually decreases after the spontaneous transition at 2.8 s. This decrease in Z_{eff} is consistent with an increase in the thermal neutron rate, calculated by the TRANSP code.

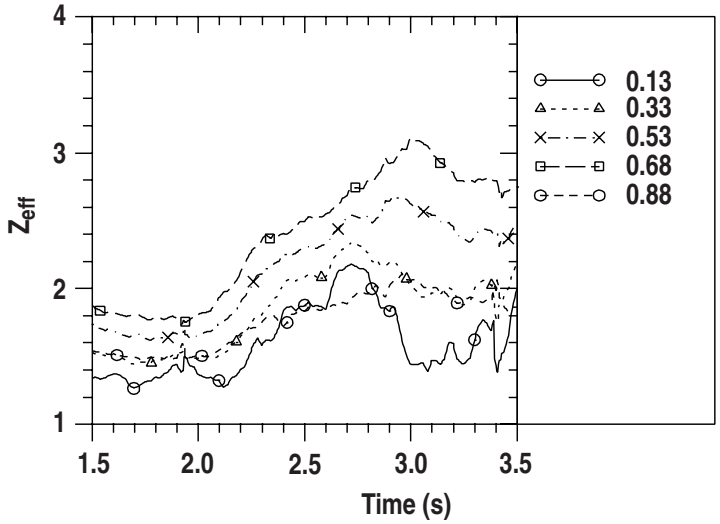

Fig. 11. Z_{eff} evolution calculated from the TRANSP code (#95011). Symbols are used to identify different curves and do not represent discrete time calculations.

The MIST 1-D impurity transport code [20] has been used to calculate radiated power from all charge states of argon, carbon, and oxygen using measured electron density and temperature profiles and SPRED UV impurity line intensities. Agreement with bolometric measurements, shown in Fig. 12(a), is very good. Nearly all of the radiation inside the LCFS occurs in the region $2/3 < \rho < 1$. Radiation profiles for the two times before and after the spontaneous transition are shown in Fig. 12(b). Even after impurity injection, radiation in confined to the mantle region.

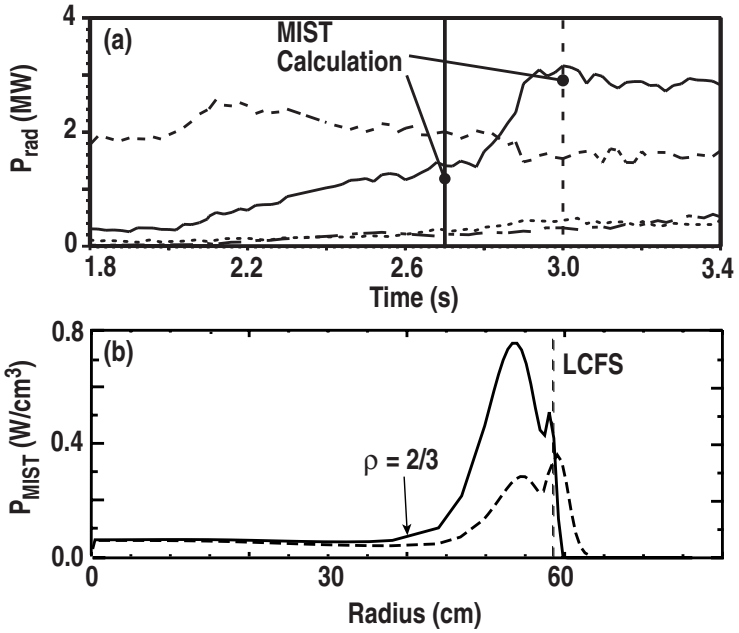

Fig. 12. Radiated power in various regions: $\rho < 1/3$ (dotted line), $1/3 \rho < 2/3$ (dash-dot), $2/3 < \rho < 1$ (solid) and divertor (dashed) for discharge #95011, (a). MIST calculations of radiated power integrated from $2/3 < \rho < 1$ at two times (solid and dashed vertical lines), before and after the spontaneous transition are also shown. Radiated power profiles calculated from the MIST code for these two times are plotted in (b); 2.7 s (solid line) and 3.0 s (dashed line).

E. MHD activity in puff and pump discharges

Nearly all puff and pump impurity seeded discharges exhibit n=2 MHD activity which limits the highest density and magnetic stored energy. Analysis of the MHD in a discharge with the same characteristics as #95011 (discussed previously) is displayed in Fig. 13. This discharge was selected because the fast time domain magnetic data was available during the onset of the mode. Modal analysis identifies the activity as m=3, n=2 and its onset occurs just after $\Delta'r$ becomes less negative, i.e. more unstable [Fig. 13(d)]. $\Delta'r$ is calculated from the code TEAR [21] using EFIT equilibria as input. In the case shown in Fig. 13, $\Delta'r$ increases in amplitude before each sawtooth crash, shown

as a negative spike in Fig. 13(c), until at t = 3.06 s the 3/2 tearing mode becomes unstable. This mode is identified as a neoclassical tearing mode where the helically perturbed bootstrap current from the q=1 sawtooth coupling to q = 3/2 excites the unstable mode. The resulting sawtooth reconnection can provide the necessary seed island and, in fact, the 3/2 mode is observed to begin increasing in amplitude within 0.02 s after a sawtooth crash. Although sawteeth are not always the trigger for the increase in 3/2 MHD activity, n=2 modes are observed in all types of impurity seeded discharges and usually limit the maximum density and confinement achieved.

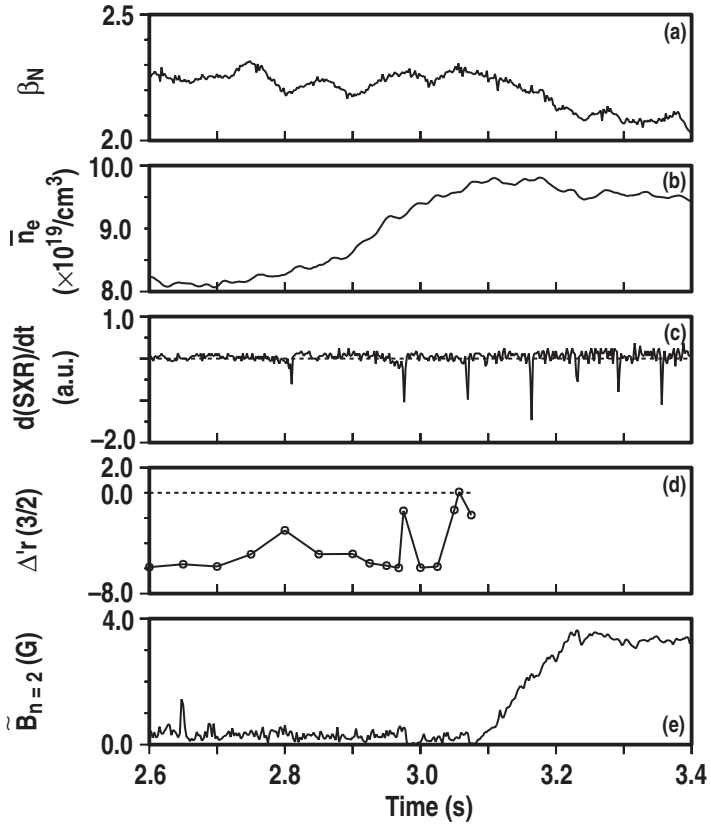

Fig. 13. Normalized β (a) and electron density (b) decrease after the onset of n=2 MHD activity. Before the first 3 sawteeth, shown by the time derivative of a central soft x-ray channel (c), Δ'r becomes successively more positive, i.e. unstable (d) until MHD activity commences (e). Δ'r is calculated from the TEAR code.

F. Differences between radiating mantle and radiating divertor discharges

In the preceding discussion radiating mantle discharges have been compared to ones with predominantly divertor radiation. These represent the two extremes for impurity seeded puff and pump scenarios. The effect of varying the rate of argon impurity injection is shown in Fig. 14. The normalized edge toroidal current density at $\rho = 0.95$, j_{t95N},

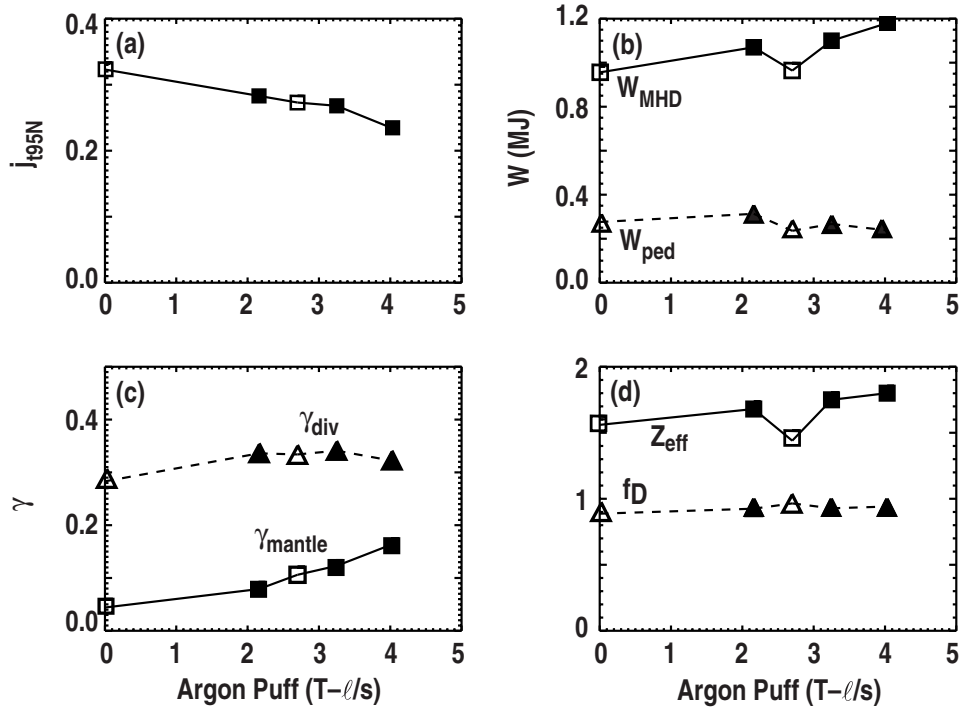

Fig. 14. Impurity puff scan for five discharges with similar characteristics: I_p = 1.3 MA, B_T = 2.1 T, P_{NB} = 12 MW. Parameters are calculated at t = 2.6 s: (a) normalized edge current density from EFIT reconstructions with MSE, (b) W_{MHD} and $W_{pedestal}$, (c) divertor and mantle radiated power fractions, and (d) core Z_{eff} and deuteron fraction, f_D. Discharges with n=2 MHD activity during or immediately before t = 2.6 s are shown as open symbols. A constant argon gas injection rate commenced at 2.0 s.

monotonically decreases with increasing argon [Fig. 14(a)] and is unaffected by the presence of n=2 MHD activity, shown as open symbols. This current density is determined with the EFIT magnetic equilibrium code including motional Stark effect (MSE) measurements. Internal inductance, ℓ_i, shows little change (not plotted) but the fraction of mantle radiation increases by nearly a factor of two at the highest argon puffing rates, shown in Fig. 14(c). There is also an increase in stored energy with impurity injection, shown in [Fig. 14(b)] except for the discharge where an n=2 mode was present. However, the pedestal energy, W_{ped}, is nearly constant. For this scan there is only a small increase in the central Z_{eff} [Fig. 14(d)] as the argon flow rate is increased and only a small decrease in the fraction of core deuterons, f_D, inferred from the SPRED UV spectrometer and electron density profiles, where f_D is defined as $f_D = 1 - \sum n_i Z_i / n_e$. The data in Fig. 14(d) is only at 2.6 s and these discharges are evolving. At later times discharges with n=2 MHD activity can lead to higher core Z_{eff}, up to 2.5.

III. IMPURITY SEEDING IN L–MODE DISCHARGES

A goal of this work is to extend the results of the TEXTOR RI–mode to larger devices such as DIII–D and also to different configurations such as a divertor. In this section we will discuss L–mode discharges with enhanced confinement comparable to H–mode. Such discharges have been obtained in both a limiter and divertor configuration, at densities lower than the puff and pump discharges in Section II. First IWL L–mode discharges are presented and then USN L–mode diverted discharges, with more complete diagnostic coverage, are analyzed.

A. IWL L-mode discharges with impurity seeding

The TEXTOR RI–mode has an L–mode edge, a nearly circular cross section, and is limited by the ALT–II pumped limiter on the outboard radius [22]. Similar shapes have been achieved in DIII–D, with the exception that DIII–D discharges are limited on the inner graphite tiled centerpost. Some DIII-D discharges do exhibit behavior qualitatively similar to the TEXTOR RI–mode, e.g. Fig. 15. In this discharge, neutral beam heating was applied at about the time of current flattop, 1 s. The confinement enhancement, H_{89P}, (not shown) was ~1.2, or nearly L–mode until shortly after neon injection at 1.2 s. At this point, magnetic stored energy, W_{MHD}, density, and radiated power [Fig. 15(a) and 15(b)] begins increasing until the onset of sawtooth activity at 1.75 s. After this time, density and radiated power continued rising (there was no active pumping of this discharge), but W_{MHD} became nearly constant and then slowly decreased. The total D_α and CIII line intensities, inferred from a 16 channel filterscope array for an IWL DIII–D discharge, are shown in Fig. 15(c) and 15(d). After neon injection, there is a prompt drop in D_α and CIII intensity and then D_α emission steadily decreases. With the onset of sawteeth at 1.76 s, the CIII intensity also decreases.

For DIII–D IWL discharges an absolute calculation of particle confinement time is difficult due to the limited diagnostics observing the inner wall. Nevertheless an estimate can be made from the D_α flux using the Johnson and Hinnov relation $\Gamma_{DR}/\Gamma_{D_\alpha}{}^{tot} \approx 15$ [23], where Γ_{DR} is the recycling flux. The total D_α emission is given by

$$D\alpha^{tot} = \int D\alpha \, dS \tag{4}$$

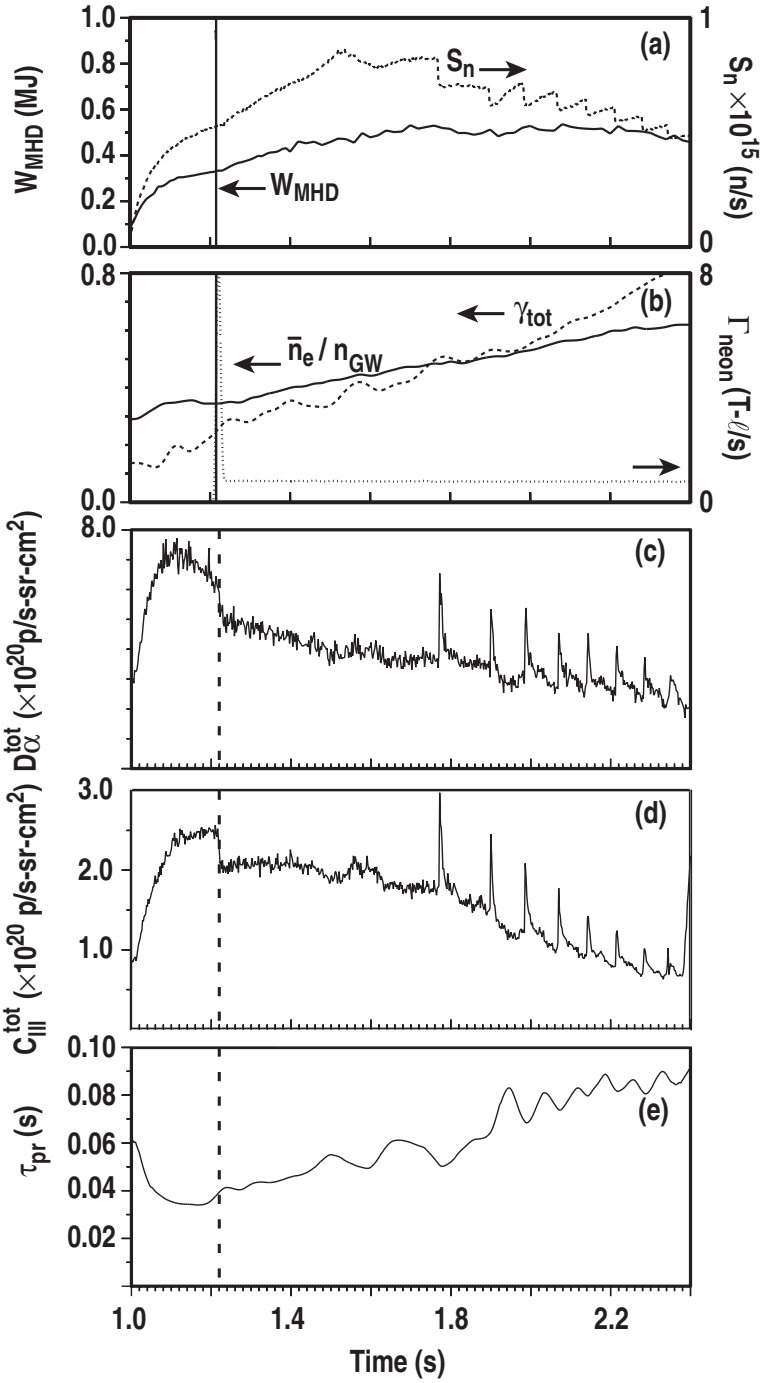

Fig. 15. Stored magnetic energy (a) increases for an IWL L–mode discharge (#98347) after neon injection (b) beginning at 1.22 s. The neutron rate, S_n, (a) initially increases and then remains constant until the onset of sawteeth. Both mantle radiation and density increase (b) while D_α and CIII line intensities are steadily reduced (c) and (d). Spikes in D_α and CIII correspond to sawtooth reconnection events. Relative particle confinement time [Eq. (5)] is plotted in (e). Parameters are: inner wall limited, I_p = 1.0 MA, B_T = 2.1 T, P_{NB} = 4.9 MW, κ = 1.24–1.27.

and is approximated by the D_α line emission from the 16 channel filterscope array integrated over the DIII–D vessel surface, S. Using this relation, we can then calculate a relative particle confinement time, defined as

$$\tau_{pr} = N_D/(\Gamma_{gas} + \Gamma_{NB} + \Gamma_{DR} - dN_D/dt) \quad (5)$$

where Γ_{gas} and Γ_{NB} are the external fueling rates from gas and neutral beams, and N_D is the total number of deuterons, calculated from the electron density, Z_{eff}, and plasma volume.

Plotted in Fig. 15(e) is the relative particle confinement time, τ_{pr}. There is a nearly monotonic increase in τ_{pr} after impurity injection. However, due to the assumptions discussed above, an absolute value cannot be ascribed to this measurement and in particular electron temperature at the inner wall must be included in the calculation before a more quantitative representation of particle confinement time can be made.

1. Confinement scaling of IWL L-mode discharges

The DIII–D inner wall limiter L–mode discharges most closely approximate the TEXTOR shape and edge properties, and confinement scaling, H_{93P}, as a function of normalized density for this discharge type is plotted in Fig. 16(a). The discharges represented in this figure are taken from the radiating mantle impurity database from 1997 to 1999. The solid line represents an offset linear fit to the data points. Also plotted is the TEXTOR RI–mode scaling, given by Eq. (1). Although there is scatter about the fit, there is a linear increase of confinement with density, similar to TEXTOR, but with an offset. We note that the DIII–D discharges were evolving in time, while the TEXTOR scaling was derived using quasi-stationary discharges. Furthermore, DIII–D data in Fig. 16 included some data with MARFEs and some data taken just after an H to L back transition, which may account for some of the scatter. As observed in TEXTOR, there is no apparent correlation between radiated power and normalized confinement with impurity seeding [Fig. 16(b)]. Within the range of radiated powers shown in Fig. 16, $\gamma_{tot} > 0.4$, the DIII–D data does not show a threshold for a transition to improved confinement as observed in TEXTOR where a threshold radiative power fraction, $\gamma_{tot} \approx 0.5$, has been reported [3].

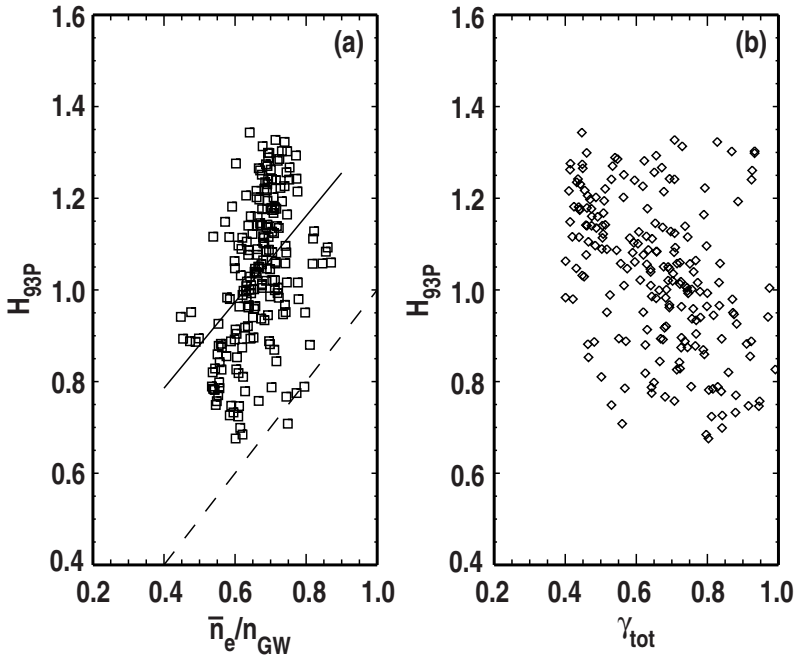

Fig. 16. Confinement enhancements from the DIII–D radiating mantle database for inner wall limited (IWL) L–mode discharges with impurity seeding in DIII–D are above the TEXTOR RI–mode scaling relation (dashed line), (a). There is no apparent correlation with γ_{tot}, (b). Points selected are: $I_p > 1.0$ MA, $\gamma_{tot} > 0.4$, during the time of impurity injection.

2. Transport in IWL discharges with impurity seeding

The effective thermal diffusivity for an IWL L–mode, a shape similar to the TEXTOR discharges, is plotted in Fig. 17. χ_{eff} decreases in the mantle region, $0.5 \leqq \rho \leqq 1.0$, after neon injection. After the onset of an n=2 MHD mode, χ_{eff} again increases although the effective thermal diffusivity in the mantle is still below the non-seeded phase. Although a detailed comparison has not been made between transport in TEXTOR RI–mode discharges and DIII–D IWL discharges qualitatively they are similar.

B. USN diverted L–mode discharges with impurity seeding

Since the mantle region plays such an important role in discharges with impurity seeding, it might be expected that the effects discussed for limiter discharges would also be observed in L–mode *diverted* discharges. In fact, enhanced confinement L–mode discharges have also been obtained in a diverted USN configuration. Such a configuration was chosen because of the higher L–H power threshold when the $\nabla\mathbf{B}\times\mathbf{B}$ drift direction is away from the X–point. (All discharges discussed in this section are L–mode.) Shown in Fig. 18 is a discharge with neon injection and a baseline discharge with deuterium injection allowing comparison at similar densities [Fig. 18(c)]. Beginning immediately after

neon injection at 1.2 s, there are marked increases in H_{93P}, the neutron rate, radiated power, and central toroidal rotation and a decrease in the total D_α line intensity plotted in Fig. 18(a,b,d,f and e) respectively.

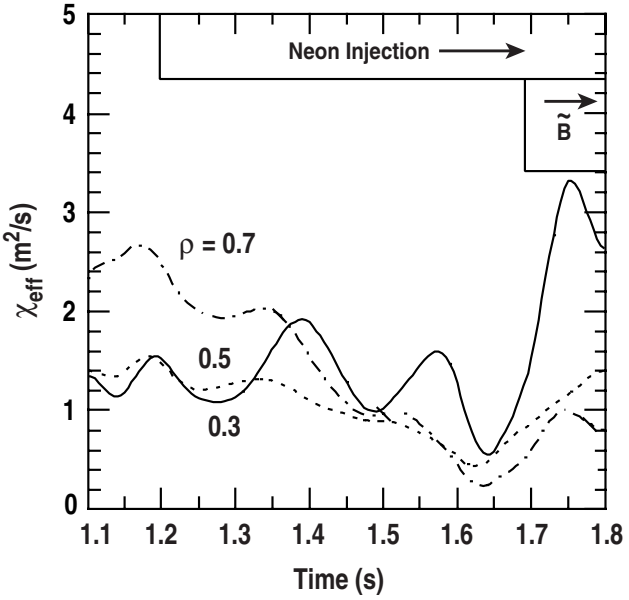

Fig. 17. χ_{eff} at three normalized radii for an RI–mode-like IWL L–mode discharge (#98795) as a function of time. The onset of n=2 MHD activity is also shown ((I_p = 1.3 MA, B_T = 2.1 T, P_{NB} = 6.8 MW).

1. USN Confinement scaling with impurity seeding and an L-mode edge

Normalized energy confinement in DIII–D USN L–mode discharges with impurity seeding is above TEXTOR scaling [Fig. 19(a)], but no correlation with either density or radiation [Fig. 19(b)] is obvious in the complete data set. However, there are clusters of points from this data set which do show a correlation. Three sets of data are plotted in Fig. 20 from two experimental days. In Fig. 20 there is a well defined linear correlation between H_{93P} and $\bar{n}_e/n_{GW}$ for two cases (diamond and x symbols) with a higher increase in confinement occurring at much lower density than reported in TEXTOR. The major difference between the two datasets with the fitted lines is that auxiliary heating power was higher and the strike point was positioned closer to the cryopump for the case at lower density. The third dataset (square symbols in Fig. 20) with no pumping does not exhibit as strong a dependence of confinement on normalized density. The discharge shape was the same as the lowest density dataset but it is not certain that pumping was the sole cause for the differences observed in Fig. 20.

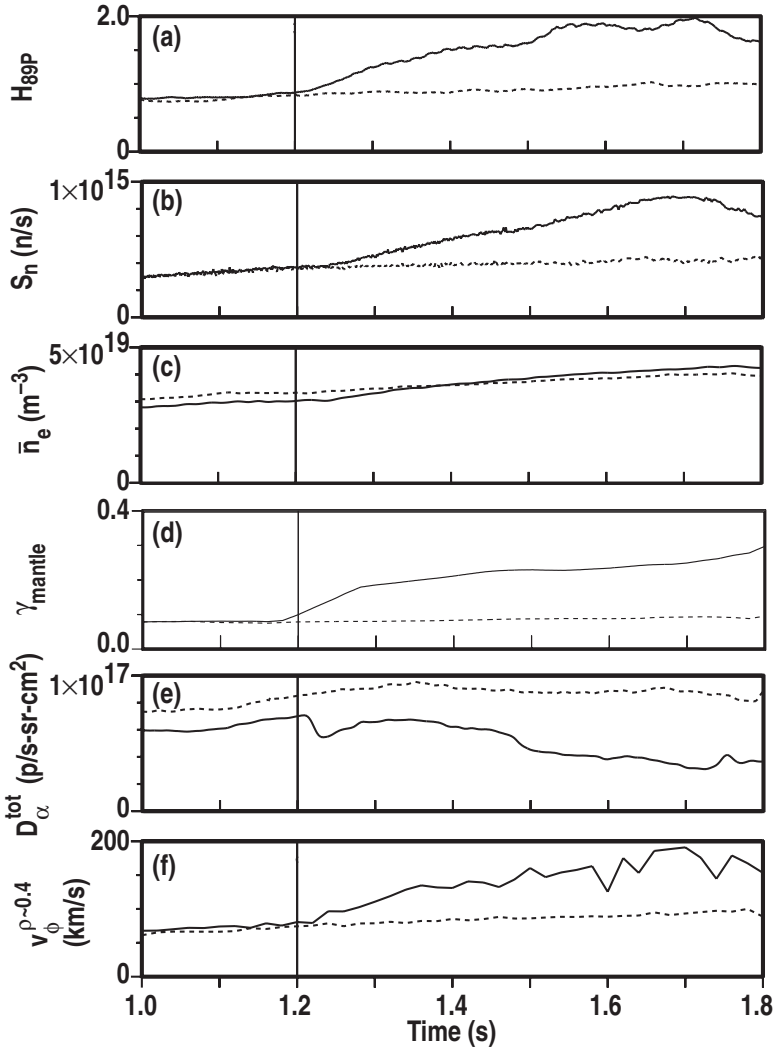

Fig. 18. Temporal response for a neon impurity seeded L–mode USN discharge, #96982 (solid lines), and a baseline discharge, #96983 (dashed lines), with deuterium gas injection to achieve approximately the same density, $\bar{n}_e$. Plotted are: (a) H_{89P}, (b) neutron emission, S_n, (c) line averaged electron density, (d) γ_{mantle}, (e) D_α line intensity, and (f) core rotation.

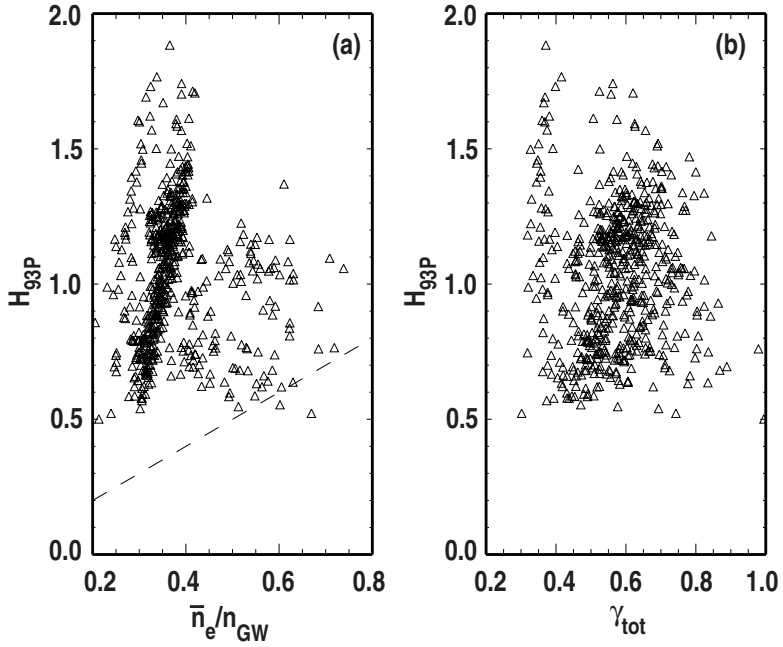

Fig. 19. Confinement enhancements from the DIII–D radiating mantle database for USN divertor L–mode discharges with impurity seeding in DIII–D are above the TEXTOR RI–mode scaling relation (dashed line), (a), but there is no apparent scaling of the entire database. Points selected are: $I_p > 1.1$ MA, $\gamma_{tot} > 0.3$, $P_{NB} > 2$ MW during the impurity puffing phase. Also shown is H_{93P} as a function of γ_{tot}, (b).

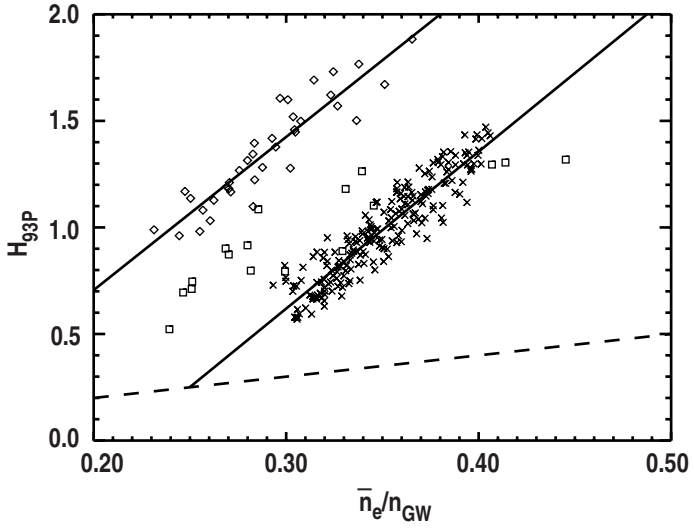

Fig. 20. A subset of the experimental points shown in Fig. 19 for two experimental days: Diamonds and squares with neon impurity seeding are from the same day (#96559–96569, $\bar{q}_{95}$ = 4.2) with and without pumping respectively. The x symbols are from another day (#99774–99794, $\bar{q}_{95}$ = 3.7) with neon, argon and krypton impurity seeding with cryopumping. Solid lines are a linear offset fit to the diamond or x symbols. TEXTOR RI–mode scaling is shown as a dashed line.

2. Transport in USN L-mode discharges

L–mode discharges with an upper single-null configuration also show a marked decrease in thermal diffusivity with impurity injection. These discharges have lower density than those described in Section II allowing calculation of χ_i and χ_e with lower uncertainties. An example for an upper single null discharge is shown in Fig. 21, and compared to a baseline non-seeded discharge. After neon injection, both χ_i and χ_e are reduced, with the largest decrease in the ion channel. This behavior is similar to the puff and pump discharge described earlier, Fig. 8, where χ_{eff} monotonically decreases, approaching neoclassical levels. The profiles for the L–mode case and a baseline discharge 0.34 s after the start of neon injection are given in Fig. 22. The electron thermal diffusivity is reduced primarily in the mantle region compared to the baseline discharge while χ_i is lower across almost the whole profile.

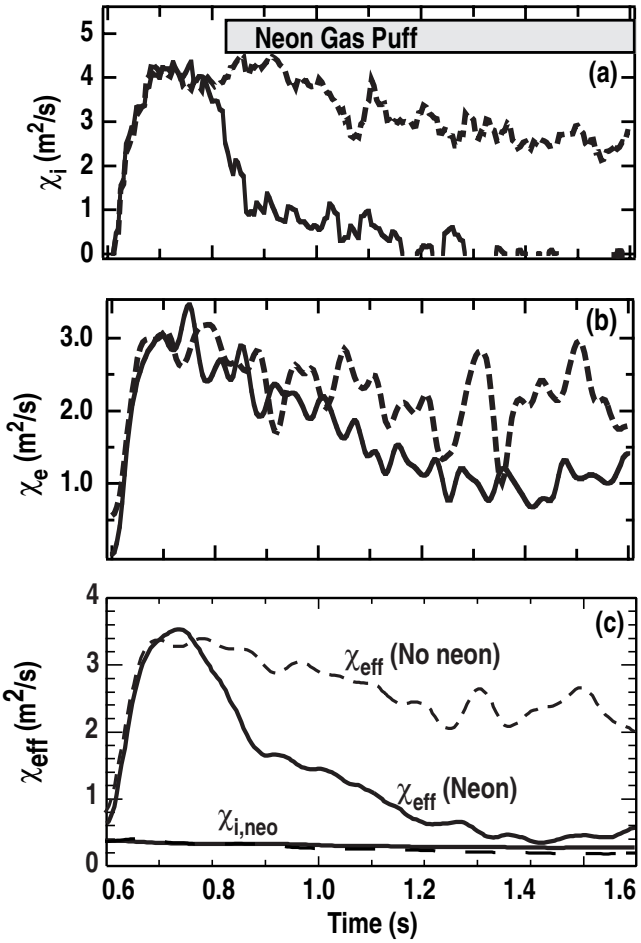

Fig. 21. Thermal diffusivities at $\rho = 0.65$ as a function of time for an L–mode USN neon seeded discharge (solid, #98777) and a baseline discharge without impurity seeding (dashed, #98775): (a) χ_i, (b) χ_e, and (c) χ_{eff} and $\chi_{i,neo}$.

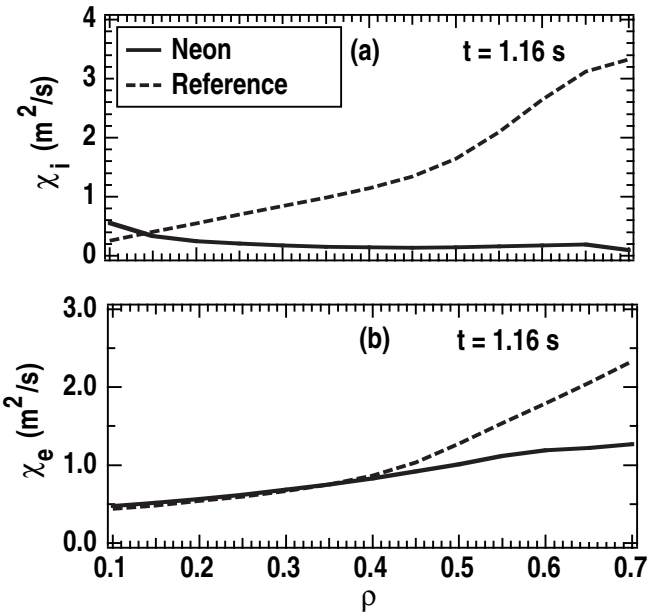

Fig. 22. Thermal diffusivity profiles for the discharges in Fig. 21 at t = 1.16 s: (a) χ_i, and (b) χ_e. From Ref. [24].

3. Edge particle fluxes in L-mode discharges

Previously an example was shown [Fig. 15] where particle confinement time increases in an IWL L–mode discharge. Since the D_α behavior is similar in IWL and USN L–mode, increased particle confinement times might be expected in both types and decreases in edge fluctuations and particle fluxes would be expected. Although measurements were not available for the series of IWL discharges in Section III.A, they have been obtained in L–mode USN diverted discharges, and are plotted in Fig. 23. The two discharges in this figure are the same as Fig. 18 and turbulent radial flux and normalized fluctuation levels are reduced by factors of 2–3 in the discharge with impurity seeding. The reduction in particle flux [Fig. 23(b)] is at least qualitatively consistent with the observed reduction in the D_α line emission. The measurements in Fig. 23 were made with a fast reciprocating probe [25] which was inserted from 1.5–1.68 s in both discharges.

4. Turbulence suppression in impurity seeded L-mode diverted discharges

We have described improvements in confinement, and decreases in transport which accompanied impurity seeding in DIII–D discharges. Here we discuss turbulence suppression in the mantle region which is a potential mechanism for explaining this behavior. The beam emission spectroscopy (BES) diagnostic [26] has measured density fluctuations for L–mode discharges with neon injection. In these discharges, BES measured the

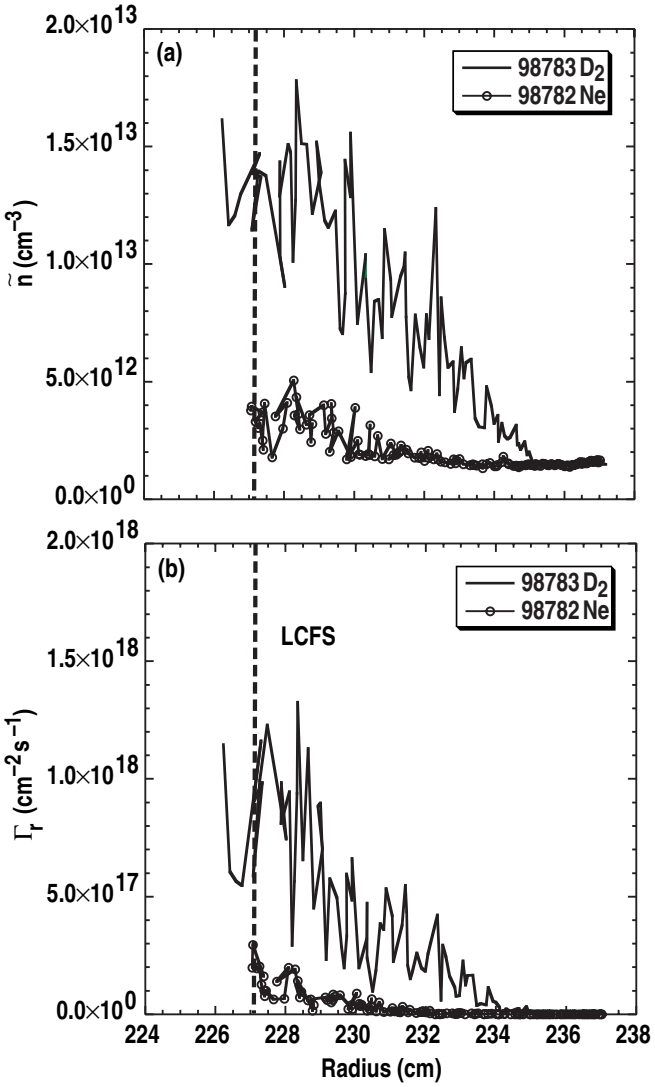

Fig. 23. RMS density fluctuation amplitude (a), and particle flux (b), measured by a fast reciprocating probe, are lower with neon seeding (#98782) when compared to a discharge with deuterium injection (#98783). Probe insertion was $1.5 < t < 1.68$ s. Discharge conditions are given in Fig. 18.

density fluctuation spectra in the wavenumber range $0.5 \leqq k \leqq 3.0$ cm^{-1}. Shown in Fig. 24 are spectra from two discharges, one with neon impurity seeding and one without. The density fluctuation spectra, Fig. 24(a), are nearly identical in both discharges before the time of neon injection. However comparing a time 0.2–0.3 s after neon injection there is a decrease in the density fluctuation spectrum, shown in Fig. 24(b), above 75 kHz ($k \approx 0.4$ cm^{-1}), and a near complete suppression of fluctuations for $f > 200$ kHz. The almost complete suppression is observed for wavenumbers $k\rho_s > 0.4$ at a radial location $\rho \approx 0.7$ [Fig. 24(b)], where $\rho_s = C_s/\Omega_i$, $C_s = \sqrt{T_e/m_i}$, and $\Omega_i = eB/m_i$ The radial profile of

neon concentration (not shown) is highest in the mantle region where BES also shows the largest reduction density fluctuations. The peak in the neon concentration occurs at $\rho = 0.53$ while the maximum reduction observed by BES is at $\rho = 0.7$ where the neon concentration is 76% of maximum. The temporal response of the fluctuations, integrated over the spectral region $0.1 < k_\perp < 0.6$ cm^{-1}, is plotted in Fig. 25. Shortly after neon injection there is a steady decrease in the fluctuations and the amplitude is significantly lower than the reference discharge.

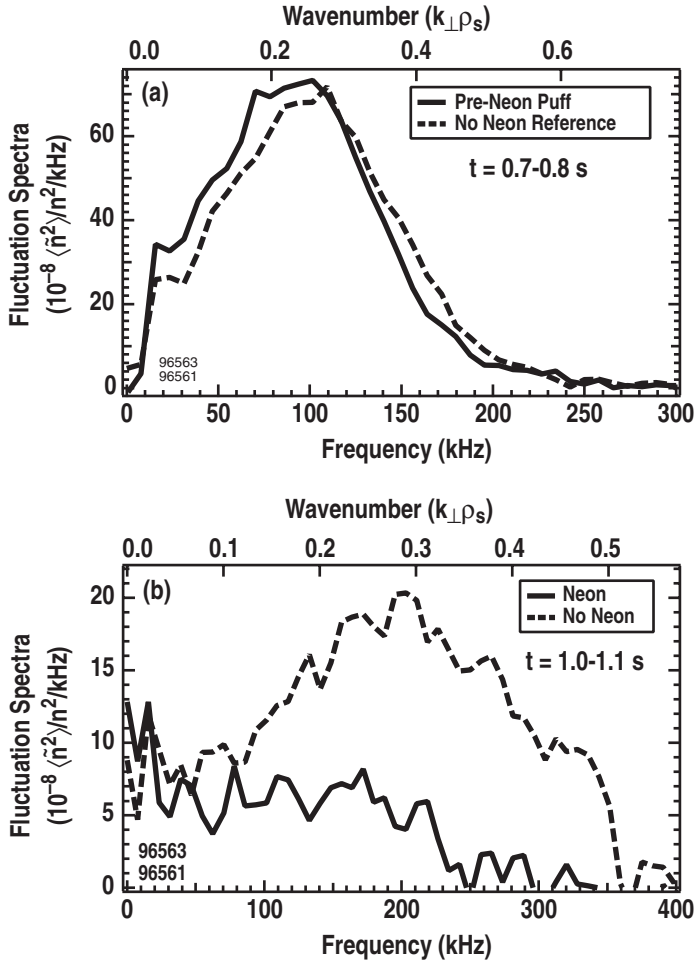

Fig. 24. Density fluctuation spectra at $\rho = 0.7$ as a function of frequency (a) before neon puffing and (b) 0.2–0.3 s after puffing. Solid line curves indicate the neon injection discharge (#96561), and dashed curves a reference discharge without neon (#96563). Discharge parameters: $I_p = 1.2$ MA, $B_T = 1.6$ T, USN divertor). From Ref. [27].

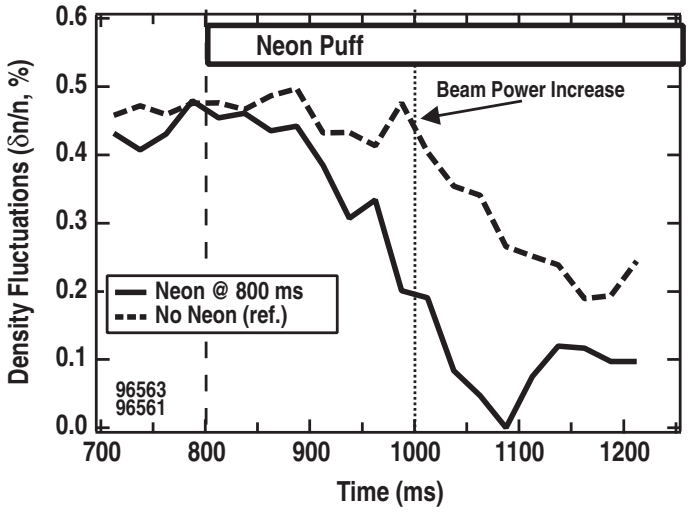

Fig. 25. Total density fluctuations at ρ = 0.7 as a function of time for the discharges in Fig. 24.

The reduction in density fluctuations with neon seeding in discharge #96561 is accompanied by a decrease in ion thermal heat diffusivity, similar to the discharge shown in Fig. 22(a), across the entire profile while electron heat diffusivity remains approximately the same. One possible mechanism for this reduction is suppression of ion temperature gradient (ITG) modes [27]. Previous studies have shown that if the **E**×**B** shearing rate is larger than the local growth rate then these turbulent modes can be suppressed. However, impurity seeding can also lower the growth rates. Gyrokinetic modeling of these discharges shows that neon injection reduces the growth rate to levels below the **E**×**B** shearing rate [27].

5. Impurities in USN L-mode discharges

Impurity concentrations and Z_{eff} are significantly higher in L–mode discharges than for puff and pump. Shown in Fig. 26(a) is the increase in Z_{eff} after neon injection into an L–mode, USN diverted discharge compared to a baseline discharge. These discharges were also shown in Fig. 18. In this case, the impurity density profile is not hollow as in the case of puff and pump discharges. Thus, although a regime of enhanced confinement is achieved, there is a rather large increase in core impurities. Note, however, that even with the higher central impurity density the neutron emission, Fig. 18(b), is still higher than the baseline discharge. This discharge with neon seeding was one of those shown in Fig. 20. No attempt has been made to date to minimize the core impurity content of these discharges. The density is well below the Greenwald density limit (Fig. 20) which may contribute to the large impurity content in these discharges.

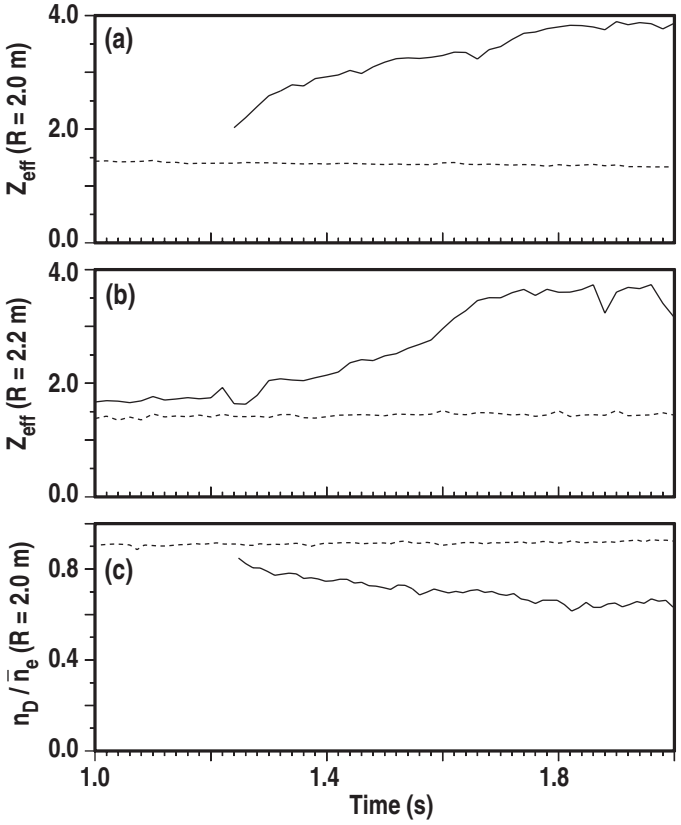

Fig. 26. Plotted is (a) Z_{eff} in the core region, (b) Z_{eff} in the mantle region, and (c) the core deuteron fraction for a radiating mantle discharge (solid, #98782) and a reference discharge (dashed, #98783). Discharge parameters are given in Fig. 18.

IV. EFFECT OF IMPURITIES IN HIGH PERFORMANCE DISCHARGES

Sections II and III focused on discharges where changes with impurity injection were observed primarily in the core and mantle regions. Impurity seeding has also been used in experiments to modify the H–mode edge region in high performance discharges, i.e. $H_{89P} > 2$. These experiments focused on either modifying ELMing behavior and extending the high performance phase or reducing the edge pedestal pressure and extending the ELM-free phases.

The effect of neon injection in an ELMing diverted discharge is compared to a reference discharge with comparable parameters in Fig. 27. Both discharges exhibited the same behavior until neon was injected into #96568 (solid curves) at 1.2 s. Both discharges remained in L–mode until 1.57 s but the impurity seeded discharge exhibited higher confinement and density [Fig. 27(a,c)]. An n=2 MHD mode began in both discharges at 1.45 s [Fig. 27(d)], but its frequency dropped rapidly in the baseline case until a locked mode occurred at t = 1.94 s. The n=2 mode in the discharge with neon injection maintained a higher frequency and the mode was localized in the core of the discharge. With impurity seeding, confinement remained above 2 for 1.5 s ($t_{dur} \approx 12\ \tau_E$) and for this time the discharge remained at or above the DIII–D empirical beta limit, $\beta_N = 4\ \ell_i$, shown in Fig. 27(b) [28]. One characteristic of these discharges is that radiation is significantly lower than the discharges discussed in Sections II and III. However γ_{mantle} in these impurity seeded discharges is still higher than non-seeded discharges, e.g. Fig. 27(c).

The ELM behavior in the two discharges described above is shown in Fig. 28. W_{MHD} is calculated using fast magnetic data for EFIT equilibria construction with a time resolution of 0.5 ms. The duration of each ELM is much longer without impurity seeding and ELM frequency is significantly lower. Energy loss per ELM, ΔW_{MHD}, is calculated by the change in W_{MHD} before and after each ELM and is greater for the baseline discharge i.e., $\Delta W_{MHD}/W_{MHD} = 0.27$ for the first ELM in the baseline discharge. In contrast the impurity seeded discharge had more frequent ELMs and $\Delta W_{MHD}/W_{MHD} \leqq 0.06$. We note that the long time between ELMs in the reference discharge is not typical of DIII–D ELMing H–mode discharges, particularly for a LSN configuration. For the two discharges in Fig. 28, early neutral beam injection was used to keep q(0) > 1 and the upper cryopump was enabled which may have affected recycling and ELM frequency. Nevertheless, both discharges had similar programming, except for impurity seeding

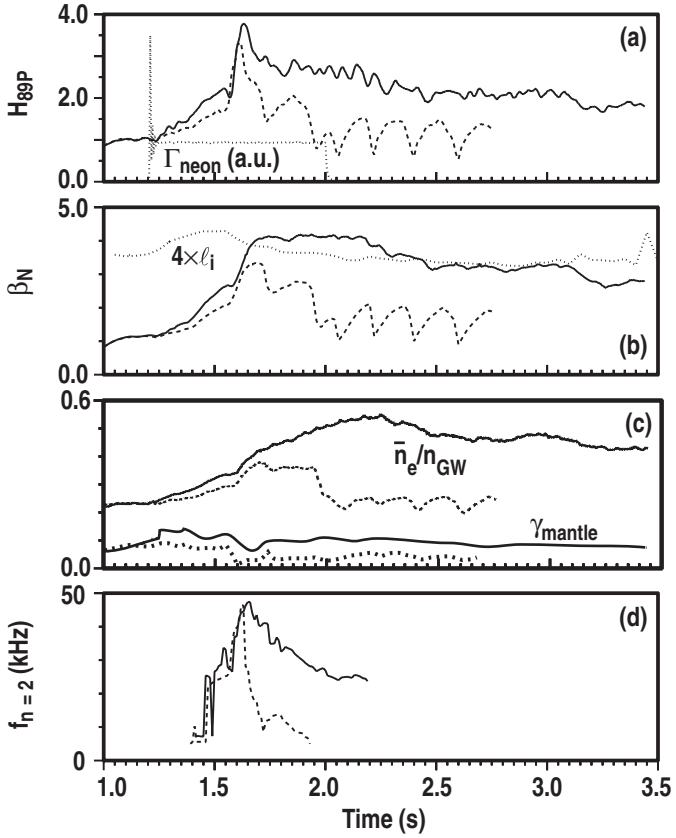

Fig. 27. ELMing H–mode discharges with neon injection (#96568, solid line) have operated at or above the empirical beta limit, 4 ℓ_i, for up to 1.4 s, (b). A comparison discharge without impurity seeding (#96970, dashed line) develops a locked mode and disrupts at 2.75 s. Also plotted are: (a) H_{89P}, (c) $\bar{n}_e/n_{GW}$ and $\gamma_{tmantle}$, and (d) frequency of the n=2 MHD mode. Parameters are: I_p = 1.2 MA, B_T = 1.6 T, P_{NB} = 11 MW, USN.

allowing a direct comparison of the effect of neon. Although not shown, both the edge pedestal pressure and edge pressure gradient *between* ELMs were similar for these discharges, despite the dramatic differences in ELM frequency and ΔW_{MHD}.

Argon and krypton have also been injected into high performance discharges to reduce the edge pedestal pressure, P_e^{ped}, and edge pressure gradients, extending the ELM-free period. An example with krypton injection is shown in Fig. 29, compared to a typical DIII–D reference VH–mode discharge [29]. Conditions were the same for both discharges, except #97899 had krypton injection. The initial high performance ELM-free phase [Fig. 29(d)] was extended in this discharge and, after a collapse to L–mode, two additional high performance phases [Fig. 29(c)] were also observed. The L–mode phases were triggered by a radiative collapse, $\gamma_{tot} > 1$ [Fig. 29(b)]. In this example, P_e^{ped} [Fig. 29(a)] reaches a lower peak value in the second and third H–mode phases of the

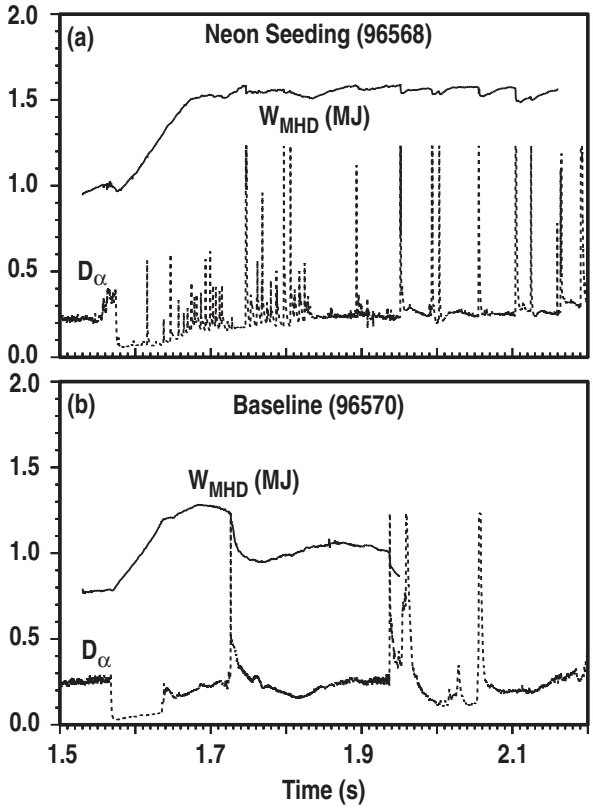

Fig. 28. W_{MHD} and D_α line intensity for two comparable discharges: (a) #96568 with neon seeding and (b) a baseline, #96570. Energy loss per ELM is higher for the non-impurity discharge (b) and a locked mode, t > 1.94 s., limits performance. Discharge parameters are given in Fig. 27.

impurity seeded discharge than in the ELM-free phase of the baseline discharge which may be correlated with the longer ELM-free periods and multiple ELM-free phases. Other krypton seeded discharges have also been obtained with even lower peak edge pedestal pressure. It is interesting to note that the radiative collapses preceding the L–mode transitions do not cause a disruption. Rather, radiated power decreases in the L–mode phases as the krypton fraction decreases until P_{LCFS} exceeds the H–mode threshold producing another high performance phase. Because the DIII–D cryopump could not be optimally positioned for pumping in these high triangularity discharges, feedback control of radiated power by varying the krypton gas puffing rate was not effective in maintaining the radiated power at a fixed level.

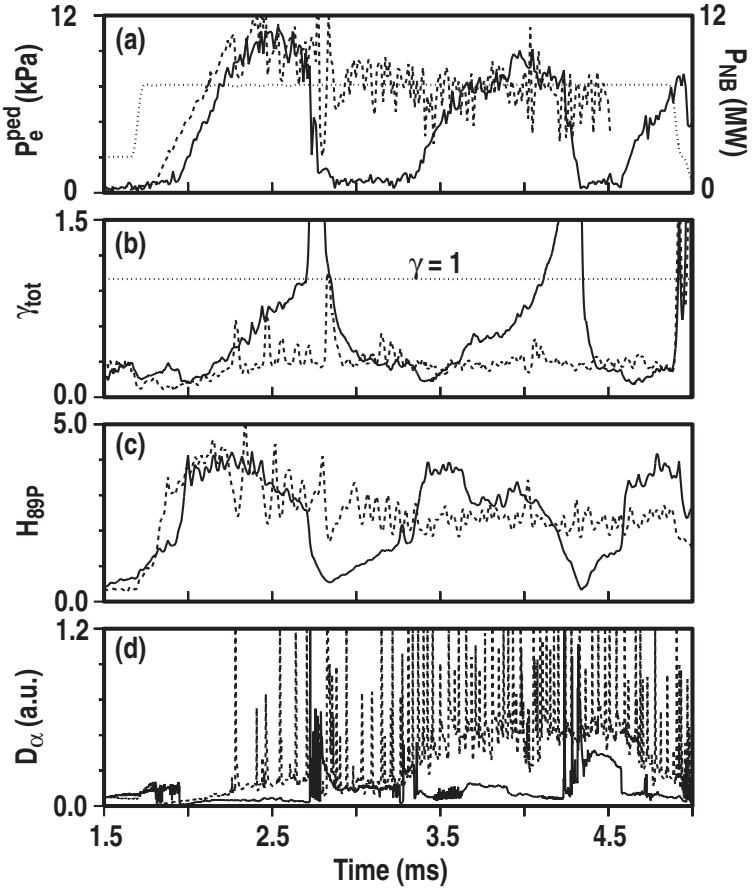

Fig. 29. Krypton injection (solid, #97899) can produce reduced edge pedestal electron pressure, (a), with VH–mode-like confinement, (c), and multiple ELM-free periods, (d) while a comparison discharge with no impurities (dash, #97886) exhibits ELMing behavior (I_p = 1.55 MA, B_T = 2.1 T,. P_{NB} = 7.4 MW, USN). L–mode periods are preceded by a radiative collapse when $\gamma_{tot} > 1$, (b).

V. DISCUSSION

A. Puff and pump discharges with impurity seeding

Impurity seeding can produce discharges with a radiating mantle and enhanced confinement under a variety of conditions. In puff and pump H–mode discharges with argon injection, $\gamma_{mantle} > 0.5$ has been obtained with energy confinement times as high as ELM-free H–mode, densities near the Greenwald density limit, and core $Z_{eff} < 2$. Nearly all were limited by the onset of n=2 MHD modes, which have been identified as 3/2 tearing modes in cases where fast magnetic data coverage overlapped the onset of these modes. Steady state discharges with somewhat lower γ_{mantle} and $\bar{n}_e/n_{GW}$ and no MHD activity have been obtained, but control of the 3/2 tearing mode remains an important problem in extending these types of discharges to higher densities under steady state conditions. Both ECH on-axis current drive and on-axis fast wave current drive are being considered to keep $q(0) > 1$, avoiding or delaying the onset of sawteeth.

For puff and pump scenarios we have focused on issues affecting the mantle and core and, in particular, discharges with a significant increase in mantle radiation. However, as noted earlier, puff and pump discharges with impurity seeding can also have a radiative divertor solution [Fig. 2(b)]. Such discharges also exhibit H–mode confinement and there appears to be no clear transition between the radiating mantle and radiating divertor states. This was illustrated in Fig. 14 where impurity puffing was varied over a series of discharges in which divertor radiation was dominant. In these discharges, W_{ped} was nearly constant and the confinement improvement occurred inside the H–mode transport barrier as the puffing rate increased.

B. L–mode discharges

L–mode operation has advantages in eliminating edge instabilities and providing an insulating mantle region and such discharges have been obtained in DIII–D both in limited and diverted configurations. L–mode impurity seeded discharges with enhanced confinement (values of H_{89P} up to 2) in both divertor and limiter configurations have been obtained in DIII–D. These discharges are evolving, usually with a steady increase in n_e, and highest density and confinement are limited by MHD activity. The USN diverted discharges were easier to establish and reproduce, possibly due to lack of MARFE activity. Although there are differences in global confinement scaling between IWL and USN

configurations, presented in Section III, there appears to be no fundamental differences in the physical mechanisms producing the improved confinement and higher density. Both types of discharges showed a decrease in χ_{eff} in a broad region, i.e. there was no sharp transport barrier. In addition, reduction in the mantle turbulence spectrum measured by BES was observed in both types of discharges.

C. High performance discharges

Impurity seeding experiments in high performance discharges have focused primarily on changing ELM characteristics and reducing edge pedestal pressure and edge pressure gradients. For these discharges, neon, argon or krypton have been injected. Neon and argon discharges exhibited small values of mantle radiation, typically $\gamma_{mantle} \leqq 0.2$, although this often represents a factor of 2 increase in mantle radiation. As shown in Fig. 15, neon injection can produce dramatic changes in ELM frequency and magnetic stored energy loss per ELM. However, edge pedestal parameters measured between ELMs exhibit only small changes.

Krypton injection has reduced the edge electron pedestal pressure gradient, extending the ELM-free high confinement phase. However the fraction of radiated power cannot be controlled and increases until a radiative collapse occurs followed by an L–mode phase. In these discharges, the lower L–mode particle confinement times allow krypton concentrations and mantle radiation to decrease until another H–mode transition occurs and another high performance phase is repeated. Up to three such cycles have been observed, limited only by the duration of the discharge. Due to weak pumping in these high performance configurations, feedback control of radiated power by varying the krypton injection rate is ineffective in avoiding the radiative collapse. A new cryopump being installed in DIII–D may provide more effective pumping of krypton, allowing feedback control of radiated power.

D. Comparison to other tokamak devices with impurity seeding

The difficulty in achieving steady state radiating mantle discharges in DIII–D is a major difference when compared to the TEXTOR RI–mode [3] and ASDEX CDH–mode [4]. Nearly circular ($\kappa = 1.3$) discharges were achieved in DIII–D, similar to the TEXTOR shape, and while marked confinement improvements are readily observed, they have not been sustained and were limited either by MARFEs or MHD activity. There are several differences between DIII–D and TEXTOR which might account for the observed differences in performance. The TEXTOR RI–mode is very sensitive to horizontal positioning of the plasma and sustained discharges can only be obtained when this has been

optimized [3]. For TEXTOR-like configurations, technical constraints presently limit DIII–D to limiter operation on the inside wall, although there does appear to be some improvement as the outer gap is decreased. Another difference between these two devices is that TEXTOR quasi-steady state RI–mode discharges generally are obtained at high density, $\bar{n}_e/n_{GW} \approx 1$, where higher collisionality can inhibit the onset of tearing modes. Although TEXTOR generally operates with the ALT–II pumped limiter, experiments have been done without pumping, similar to the DIII–D case, and RI–mode has been reproduced reliably [30]. For L–mode impurity seeded discharges, pumping can allow more effective feedback control and limit disruptions due to radiative collapse, but it is not a fundamental requirement to achieve RI–mode.

There are also differences between ASDEX–U CDH–mode and DIII–D radiating mantle puff and pump discharges. In DIII–D these discharges are not detached, as ASDEX–U reports, and DIII–D discharges have Type I ELMs [31], not the ASDEX–U Type III ELMs. Both devices report operation with H–mode confinement near the Greenwald limit for these scenarios, but as discussed previously steady state operation in DIII–D has not been demonstrated near the Greenwald density limit with impurity seeding. Although the puff and pump discharges presented in this paper are not CDH–mode, we note that CDH–mode has previously been observed in DIII–D [6].

A general feature of the TEXTOR RI–mode is the confinement scaling relation given in Eq. (1). Such a relation does not apply to the DIII–D discharges discussed in this paper. In general, confinement is higher for the same normalized density than in TEXTOR and we have observed confinement enhancements with neon impurity seeding at lower values of density and radiated power than reported by the TEXTOR group. As shown in Fig. 1, the discharge temporal evolution shows confinement improvements with increasing density, but any detailed comparisons with TEXTOR RI–mode scaling await the establishment of steady state RI–mode-like discharges. Nevertheless it is encouraging that DIII–D radiating mantle discharges are above the TEXTOR RI–mode scaling relation. An offset linear scaling relation with a strong dependence on density is apparent in two sets of L–mode data (Fig. 20) at normalized densities well below the minimum RI–mode value, $\bar{n}_e/n_{GW} \approx 0.6$, reported for TEXTOR. The extension of these results to higher values of densities, possibly by operation at lower q_{95}, is proposed for future experiments.

E. ITG mode suppression and transport in impurity seeded discharges

The leading candidate to explain improved confinement in impurity seeded discharges is the suppression of ITG driven turbulence in the mantle region. BES measurements show a clear and reproducible reduction of turbulence with impurity injection into

L–mode plasmas. Gyrokinetic modeling of these discharges indicates that the introduction of neon raises the threshold for the onset of ITG turbulence, consistent with observed reductions of fluctuations in these plasmas [27]. Similar measurements in ELMing H–mode puff and pump plasmas are difficult due to interference by ELMs and the relatively low levels of turbulence already present. However the $\mathbf{E} \times \mathbf{B}$ shearing rate does increase after impurity injection into puff and pump ELMing H–mode discharges and TRANSP modeling shows reductions in transport. Since there are only small decreases in edge pedestal pressure and W_{ped} and using the model proposed by JET [16] we conclude that the confinement improvement is coming from the core and mantle regions and not changes in the region of the H–mode transport barrier.

In both the puff and pump and L–mode discharges, there is no clear transport barrier associated with impurity seeding. Rather there appears to be a reduction in χ_{eff} and D over a large cross section of the plasma, with the largest reductions occurring in the mantle region, typically $\rho = 0.6$–0.7.

We note that the highest densities and highest confinement in both L–mode and puff and pump discharges were obtained with an increase in core toroidal rotation, although this is not a necessary condition to achieve higher densities and enhanced confinement. Increasing rotation was most noticeable at the spontaneous transition in puff and pump discharges and at the onset of impurity puffing in the L–mode discharges. This rotational shear appears to contribute to lower diffusivity and χ_{eff} and hence higher density and stored energy.

F. Impurities

One deleterious effect of impurity injection can obviously be the accumulation of impurities in the core, leading to a reduction of fusion reactivity both by dilution and cooling of the core. While this can be a concern, it appears that there are operating scenarios where this effect can be minimized, while still maintaining the desired radiation in the mantle region. As discussed in Section II, core Z_{eff} actually decreases after the spontaneous transition for puff and pump discharges, even though mantle radiation increases significantly. TRANSP modeling also shows that the thermal neutron flux increases in these discharges after this transition. Although core Z_{eff} is high in the DIII–D L–mode discharges reported here, core $n_D/n_e > 0.65$. Furthermore, the neutron emission actually increases compared to comparable discharges with only deuterium puffing, e.g. in Fig. 18 neutron emission doubles. In the experiments reported in this paper, no attempt has been made to minimize core Z_{eff}. For example, we expect that increasing the density in L–mode discharges will significantly lower core Z_{eff}.

G. SOL characteristics

As discussed previously, impurity seeding affects both the core and mantle regions. In addition, there are notable changes in the plasma SOL. In puff and pump discharges there are marked decreases in particle and heat fluxes at the outer strike point and in the SOL. This reduction is consistent with a decrease in P_{LCFS}. Although these discharges are not detached, the ELM frequency increases and the energy loss per ELM is quite low, $\Delta W_{ELM}/W_{MHD} \leqq 0.02$.

Changes in the SOL are also observed in L–mode discharges. Decreases in particle fluxes and density fluctuations measured by a reciprocating probe were shown in Fig. 23 and D_α line intensity steady decreases after impurity seeding. It is not clear whether these changes in the SOL with impurity seeding create conditions leading to improved particle and energy confinement, or if they are simply a result of changes inside the LCFS.

H. Concluding remarks

Impurity seeding in DIII–D has produced radiating mantle discharges with improved confinement and densities near the Greenwald limit. The mechanism for this improvement, at least for L–mode discharges, is consistent with a reduction in ITG induced turbulence in the mantle region and lower particle and heat diffusivities across nearly the entire profile. Normalized confinement is above the RI–mode scaling relation, and qualitatively, confinement increases with density in both puff and pump and L–mode discharges. However, additional experiments are needed to establish a scaling relation, and in particular, any possible size scaling in these types of discharges. The issue of impurities must also be addressed to assess the applicability of impurity seeding for possible reactor scenarios. In such scenarios, feedback control could be used to control impurity radiation but the minimum concentrations required to suppress ITG turbulence have yet to be established. These experiments show that impurity seeding can be effective in producing high density while maintaining confinement comparable to ELM-free H–mode. The observed decrease in power to the first wall makes the radiating mantle a candidate for reactor scenarios.

REFERENCES

[1] YUSHMANOV, P.N., TAKIZUKA, T., RIEDEL, K.S., et al., Nucl. Fusion **30**, 1999 (1990).

[2] LAZARUS, E.A., BELL, J.D., BUSH, C.E., et al., Nucl. Fusion **25**, 135 (1985).

[3] MESSIAEN, A.M., ONGENA, J., UNTERBERG, B., et al., Phys. Plasmas **4**, 1690 (1997).

[4] GRUBER, O., KALLENBACH, A., KAUFMANN, M., et al., Phys. Rev. Lett. **74**, 4217 (1995).

[5] MORI, M., et al., Nucl. Fusion **28**, 1892 (1988).

[6] JACKSON, G.L., STAEBLER, G.M., ALLEN, S.L., et al., J. Nucl. Mater. **241–243**, 618 (1997).

[7] STAEBLER, G.M., JACKSON, G.L., WEST, W.P., et al., Phys. Rev. Lett **82**, 1692 (1999).

[8] MATTHEWS, G.F., BALET, K.B., CORDEY, J.G., et al., Nucl. Fusion **39**, 19 (1999).

[9] WINTER, J., ESSER, H.G., JACKSON, G.L., et al., Phys. Rev. Lett. **71**, 1549 (1993).

[10] ONGENA, J., and A. MESSIAEN, et al., Proc. 20th Euro. Conf. on Controlled Fusion and Plasma Physics, 1993, Liscon, Portugal (European Physical Society, Petit-Lancy, Switzerland, 1993) Vol. 17C, Part I, p. 32.

[11] UNTERBERG, B., BRIX, M., JASPERS, R., et al., J. Nucl. Mater. **266–299**, 75 (1999).

[12] ITER H–Mode Database Working Group, Nucl. Fusion **34,** 131 (1994).

[13] GREENWALD, M., TERRY, J.L., WOLFE, S.M., and EJIMA, S., Nucl. Fusion **28**, 2199 (1988).

[14] WADE, M.R., WEST, W.P., WOOD, R.D., et al., J. Nucl. Mater. **266–299**, 44 (1999).

[15] GROEBNER, R.J., and OSBORNE, T.H., Phys. Plasmas **4**, 1800 (1998).

[16] FISHPOOL, G.M., Nucl. Fusion **38**, 1373 (1998).

[17] TAYLOR, T.S., Plasma Phys. and Contr. Fusion **39**, B47 (1997).

[18] GOLDSTON, R.J., et al., J. Comput. Phys. **43**, 61 (1981).

[19] BURRELL, K.H., Phys. Plasmas **4**, 1499 (1997)

[20] HULSE, R.A., Nucl. Technol./Fusion **3**, 259 (1983).

[21] HEGNA, C.C., CALLEN, J.D., et al., Phys. Plasma **1**, 2307 (1994).

[22] GOEBEL, D.M., CONN, R.W., CORBETT, W.J., et al., J. Nucl. Mater. **162–164**, 115 (1989).

[23] JOHNSON, L.C., and HINNOV, E., J. Quant. Spectrpsc. Radiat. Transf. **13**, 333 (1973)

[24] MCKEE, G.R., MURAKAMI, M., BOEDO, J.A., et al., Phys. Plasmas **7**, 1870 (2000).

[25] BOEDO, J.A., GRAY, D., CHOUSAL, L., and CONN, R., Rev. Sci. Instr. **69**, 2663 (1998).

[26] MCKEE, G.R., ASHLEY, R., DURST, R., et al., Rev. Sci. Instru. **70**, 913 (1999).

[27] MCKEE, G.R., BURRELL, K.H., FONCK, R., et al., Phys. Rev. Lett. **84**, 1922 (2000)

[28] STRAIT, E.J., Phys. Plasmas **1**, 1415 (1994).

[29] HOLTROP, K.L., JACKSON, G.L., KELLMAN, A.G., et al., J. Vac. Sci. Tech A **15**, 678 (1997).

[30] ONGENA, J., private communication (1997).

[31] DOYLE, E.J., GROEBNER, R.J., BURRELL, K.H., et al., Phys. Fluids B **3**, 2300 (1991).

ACKNOWLEDGMENTS

This is a report of work supported by the U.S. Department of Energy under Contract Nos. DE-AC03-99ER54463, DE-AC05-96OR22464, W-7405-ENG-48, DE-AC04-94AL85000, and Grant Nos. DE-FG03-95ER54294 and DE-FG02-92ER54139